THESIS FOR THE DEGREE OF DOCTOR OF PHILOSOPHY

Quantitative NanoSIMS provides subcellular concentration and distribution of oligonucleotide therapeutics

Cécile Becquart

UNIVERSITY OF GOTHENBURG

Department of Chemistry and Molecular Biology

Gothenburg, 2023

Thesis for the Degree of Doctor of Philosophy

Cover illustration: A drug concentration at its site of action within cells is an important missing piece in pharmacology. Measuring the intracellular concentration of a drug allows one to link its potency with different pharmacokinetic parameters like plasma concentration and tissue exposure, by Cécile Becquart

Quantitative NanoSIMS provides subcellular concentration
and distribution of oligonucleotide therapeutics
© Cécile Becquart 2023
Cecile.becquart@gu.se

ISBN 978-91-8069-293-9 (PRINT)
ISBN 978-91-8069-294-6 (PDF)
Available online at http://hdl.handle.net/2077/76006

Department of Chemistry and Molecular Biology
University of Gothenburg
SE-405 30 Göteborg, Sweden

Printed in Borås, Sweden 2023
Printed by Stema Specialtryck AB

ABSTRACT

Antisense oligonucleotides (ASOs) represent a powerful therapeutic modality that can selectively modulate gene expression. However, ASOs face two major hurdles that restrict their use in the clinic. The first issue is delivery of the ASO to a tissue of therapeutic interest while reducing exposure to unrelated tissues. Additionally, inefficient escape of ASOs from endolysosomal compartments affects their activity since ASOs are unable to reach their intracellular RNA target in the nucleus and/or cytosol. Despites the variety of chemical modifications developed to tackle these delivery issues, it remains challenging to reach particular tissues and/or cell types outside of the liver, and there are still no non-toxic solutions to the endosomal escape problem.

To fully realize the therapeutic potential of this class of molecules, it is crucial to understand the mechanisms underlying how ASOs enter cells and exit the endosomal space. Therefore, this thesis focuses on the use of nanoscale secondary ion mass spectrometry (NanoSIMS), in combination with electron microscopy, to investigate the subcellular distribution and accumulation of ASOs.

It was necessary to develop a NanoSIMS method capable of absolute quantification of the intracellular exposure of ASO. Thus, external standards were developed to quantify several halogenated compounds (iodide, bromide, and fluoride) as well as a sulfur isotope (^{34}S).

Results showed that the uptake of different ASOs was saturable, but conjugation to a *N*-acetylgalactosamine targeting domain enhanced cellular uptake and improved target knockdown. NanoSIMS data also showed that upon colchicine treatment, the uptake and localization of ASOs were affected. It was also possible to quantifying both the targeting domain and ASO components of an engineered glucagon-like peptide 1 ASO conjugate. That highlighted that fine tuning of ASO chemistry can be used to affect the productive uptake of ASOs.

Overall, these findings contribute to a better understanding of the cellular delivery, uptake and trafficking mechanisms of ASOs, which is valuable for the future development of more effective oligonucleotide-based therapeutics.

SAMMANFATTNING PÅ SVENSKA

Antisensoligonukleotider (ASO:er) representerar en kraftfull terapeutisk modalitet som selektivt kan modulera genuttryck, men ASO:er står inför två stora hinder som begränsar deras kliniska användning. Det första hindret är transport av ASO till en vävnad av terapeutiskt intresse samtidigt som exponeringen av icke-relaterade vävnader minimeras. Dessutom försämrarineffektiv frisättning av ASO:er från endolysosomen deras aktivitet, eftersom ASO:er då inte kan nå sitt intracellulära RNA-mål i kärnan och/eller cytosolen. Trots att flertalet olika kemiska modifieringar har utvecklats för att adressera dessa problem, är det tyvärr fortfarande utmanande att nå särskilda vävnader och/eller celltyper bortsett levern, och det finns fortfarande inga icke-toxiska lösningar för endosomal frisättning.

För att fullt ut utnyttja den terapeutiska potentialen hos denna klass av molekyler är det avgörande att förstå mekanismerna bakom hur ASO:er går in i celler och frisätts från endosomen. Denna avhandling fokuserar på användningen av sekundär jonmasspektrometri i nanoskala (NanoSIMS), i kombination med elektronmikroskopi, för att undersöka subcellulär distribution och ackumulering av ASO:er.

Det uppstod ett behov att utveckla en NanoSIMS-metod som kunde kvantifiera absoluta nivåer av den intracellulära exponeringen av ASO:er. Därför utvecklades flera externa standarder för att möjliggöra kvantifiering av flera halogenerade föreningar (märkta med jodid, bromid och/eller fluorid) samt en svavelisotop (^{34}S).

Resultaten visade att upptaget av olika ASO:er var mättat, men konjugering till en *N*-acetylgalaktosamin förbättrade både cellulärt upptag och effekten av samtliga testade ASO:er. NanoSIMS-data visade också att vid behandling med kolkicin påverkas upptaget och lokaliseringen av ASO:er i cellen. NanoSIMS användes också för att kvantifiera båda komponenterna i ett konstruerat glukagonliknande peptid 1-ASO-konjugat i subcellulära områden. Detta visade att finjustering av ASO-kemin kan användas för att påverka det produktiva upptaget av ASO:er.

Sammantaget bidrar dessa fynd till en bättre förståelse av ASO-transport till celler, dess upptagsmekanismer samt intracellulär transport, vilket är värdefullt för den framtida utvecklingen av mer effektiva oligonukleotid-baserade läkemedel.

List of publications and contribution report

I. Intracellular Absolute Quantification of Oligonucleotide Therapeutics by NanoSIMS.

Cécile Becquart, Rouven Stulz, Aurélien Thomen, Maryam Dost, Neda Najafinobar, Anders Dahlén, Shalini Andersson, Andrew G. Ewing, Michael E. Kurczy. *Analytical Chemistry*, 2022, 94(29), 10549-10556

Designed and performed the experiments and interpreted the data. Outlined and wrote the first draft of the paper. Edited the manuscript with the other authors.

II. Nanoscale secondary ion mass spectrometry quantification of targeted drug delivery of nucleic acid-based therapeutics: The GalNAc benchmark.

Cécile Becquart, Quentin Vicentini, Rouven Stulz, Anders Dahlén, Samir El Andaloussi, Constanze Hilgendorf, Shalini Andersson, Andrew G. Ewing, Michael E. Kurczy. Submitted

Participated in designing the experiments, performed the experiments related to NanoSIMS and interpreted the data. Participated in data discussion. Outlined and wrote the first draft of the paper. Edited the manuscript with the other authors.

III. Understanding antisense oligonucleotide trafficking with NanoSIMS: quantification of the colchicine effect.

Cécile Becquart, Dennis Hekman, Constanze Hilgendorf, Shalini Andersson, Andrew G. Ewing, Michael E. Kurczy. Manuscript.

Designed and performed the experiments. Interpreted the data, participated in data discussion, outlined and wrote the first draft of the paper. Edited the manuscript with the other authors.

IV. NanoSIMS Imaging Reveals the Impact of Ligand-ASO Conjugate Stability on ASO Subcellular Distribution.

Emma Kay, Rouven Stulz, Cécile Becquart, Jelena Lovric, Carolina, Tängemo, Aurélien Thomen, Dženita Baždarević, Neda Najafinobar, Anders Dahlén, Anna Pielach, Julia Fernandez-Rodriguez, Roger Strömberg, Carina Ämmälä, Shalini Andersson, Michael E. Kurczy. *Pharmaceutics*, 2022, 14(2), 463-481.

Designed and performed the NanoSIMS experiment related to the GalNAc-ASO as well as analyzed and interpreted the data. Participated in data discussion and editing the manuscript with other authors.

Related paper not included in the thesis

I. Elevated Adipocyte Membrane Phospholipid Saturation Does not Compromise Insulin Signaling.

Henrik Palmgren; Kasparas Petkevicius; Stefano Bartesaghi; Andrea Ahnmark; Mario Ruiz; Ralf Nilsson; Lars Löfgren; Matthew S. Glover; Anne-Christine Andréasson; Liselotte Andersson; Cécile Becquart; Michael Kurczy; Bengt Kull; Simonetta Wallin; Daniel Karlsson; Sonja Hess; Marcello Maresca; Mohammad Bohlooly-Y; Xiao-Rong Peng; Marc Pilon. *Diabetes*, 2022.

Participated in designing and performing the experiments related to NanoSIMS. Interpreted the data and participated in data discussion. Participated in editing the manuscript with the other authors.

Table of contents

ABBREVIATIONS

ADME	Absorption, distribution, metabolism and excretion
AP-MALDI	Atmospheric pressure matrix-assisted laser deorption ionization
ASGPR	Asialoglycoprotein receptor
ASO	Antisense oligonucleotide
BNA	Bridged nucleic acids
CDT	Canyon Diablo Troilite
cEt	Constrained 2'-O-ethyl
DESI	Desorption electrospray ionization
DNA	Deoxyribonucleic acid
EE	Early endosome
eGLP1	Engineered glucagon like peptide 1
ELISA assay	Enzyme-linked immunosorbent
EM	Electron microscopy
GalNAc	*N*-acetylgalactosamine
GLPR	Glucagon like peptide 1 receptor
LC-MS	Liquid chromatography coupled to mass spectrometry
LE	Late endosome
LNA	Locked nuclei acid
LOD	Limit of detection
LOQ	Limit of quantification
m/z	mass-to-charge ratio
MALAT1	Metastasis-associated lung adenocarcinoma transcript 1
MALDI	Matrix-assisted laser deorption ionization
mRNA	Messenger RNA
MSI	Mass spectrometry Imaging
nanoDESI	nanospray desorption electrospray ionization
NanoSIMS	Nanoscale secondary ion mass spectrometry
ncRNA	non-coding RNA
ONT	Oligonucleotide therapeutics
PO	Phosphodiester
PS	Phosphorothioate
qMSI	Quantification by MSI
RNA	Ribonucleic acid
RNase H	Ribonuclease H
RSF	Relative sensitivity factor
RT-qPCR	Reverse-transcriptase quantitative polymerase chain reaction
SEM	Scanning electron microscopy
SIMS	Secondary ion mass spectrometry
siRNA	Small interfering RNA
TEM	Transmission electron microscopy
TOF	Time of flight
VPDB	Vienna Pee Dee Belemite

Chapter I. Mass Spectrometry Imaging (MSI) in the pharmaceutical landscape.

1.1. Introduction

It is essential for a drug to reach its biological target at adequate concentration in order to have an effect. In this instance the term target refers to the biomolecules (DNA, RNA and proteins) that are responsible for the therapeutic effect of the drug.[1, 2] Thus, the ability of a drug to produce the desired effect or to elicit an adverse effect necessarily needs to be contextualized in terms of concentration at site of action. In the pharmaceutical field, drug concentration at site of action is most often reflected by plasma concentration. However, as a large number of drugs have intracellular targets, those measurements can lead to a poor representation of the drug exposure and efficacy.[3] The effects of drug absorption, distribution, metabolism, and excretion (ADME) processes that take place within the human body must also be considered.[4, 5] This implies that the drug may reach different organs but also different tissues and cells within a specific organ where it will be transformed into metabolites (active or not) then can be eliminated from the body, and this will affect its efficacy and safety profile.

Therefore, it is important to visualize the drug distribution *in vivo* or *in vitro*. Several methods are used by pharmaceutical companies to assess the presence and localization of a drug.[6] In preclinical research, autoradiography is used to visualize radiolabeled drugs and track their distribution and metabolism in a biological sample.[7, 8] This allows to identify where the drug acts in the body and study its ADME properties to provide invaluable pharmacokinetics and pharmacodynamics information.[9] Fluorescence microscopy can also be used via incorporation of a fluorescent tag on the compound of interest to provide its localization with high lateral resolution.[6, 10] However, it is not always possible to readily introduce a fluorophore on the drug and addition of this moiety can also change its chemical and biological properties.[11, 12] Other imaging techniques like magnetic resonance imaging, computed tomography and position emission tomography can be used to visualize the distribution of drugs in the body.[13, 14] Biomarker molecules can also be indicators of a drug presence and localization [15]. Another rough way to assess the presence and localization of a drug substance can be done by extracting the compound from specific tissue homogenate and analyzing it by liquid chromatography coupled to mass spectrometry.[16]

Some of these techniques require labeling of the drug compound which can be discouraging for one or all of the following reasons. The synthesis can be technically challenging and time consuming the starting materials may be costly [6, 17], and finally may not provide the distribution information at the appropriate level. This encouraged pharmaceutical companies to add mass spectrometry imaging (MSI) to their tool box. MSI is a powerful technique that allows for the spatial visualization of the abundance and distribution of different molecules of a sample. In the pharmaceutical industry, MSI has different applications.[18-22] It can be used in the quality control and formulation development by imaging the distribution of the active ingredient of the drug as well as excipients in the tablets. [23] MSI can also be used to study the distribution and metabolism of a drug in *in vivo* model organisms like mice.[24, 25] It is then possible to get information in the earliest stages of drug discovery, to study the distribution of drug candidates in diseases tissue providing insight into their therapeutic effect(s) and mode of action.

1.2. Overview of mass spectrometry imaging

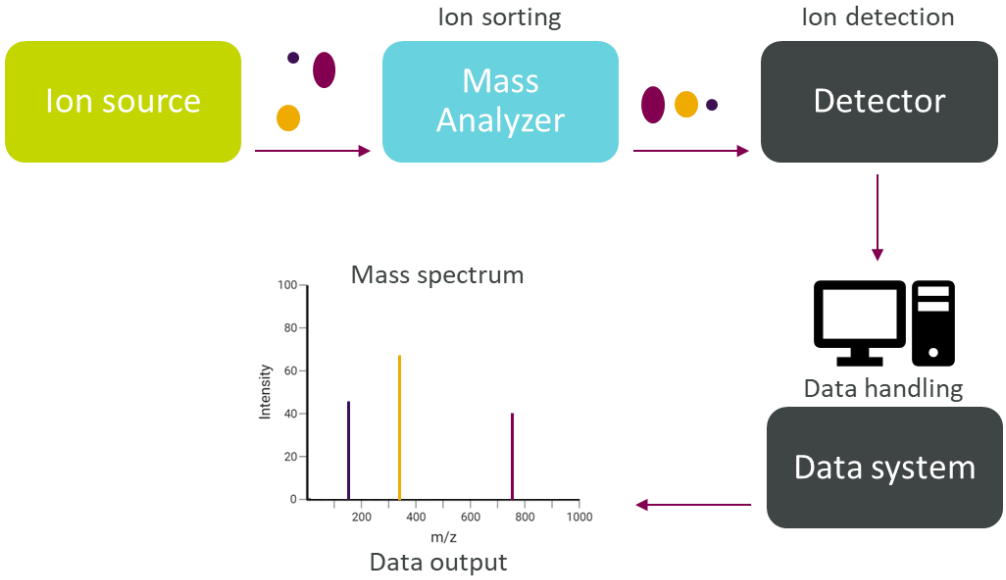

Figure 1. Basic schematic of a mass spectrometer. The sample is ionized via the ion source and gas-phase ions are produced. The charged species are separated in the mass analyzer according to their mass-to-charge ratio (m/z). The relative abundances of the detected ions are converted in electric signals further transmitted to a computer to generate a mass spectrum of the sample.

MSI is a technique used to create images of the distribution of specific molecules within a sample. The sample is typically a thin section of tissue or cell but can also be a material surface or a liquid droplet. MSI encompasses a broad range of mass spectrometry-based instruments that offer various capabilities with their own advantages and limitations.[26-31] Regardless of the mass spectrometry technique, molecules of the sample first undergo ionization where they are transformed into gas-phase ions (Figure 1). Then a mass analyzer separates the ions based on their mass-to-charge ratios (m/z).[32] The separated ions are then detected together with the abundance of the different molecules in the sample as a function of their m/z. The resulting mass spectra are then used to create an image of the distribution of a specific molecule or group of molecules within the sample (Figure 2). The pairing of the ionization source and mass analyzer determines which molecules (small-molecules, lipids, peptides, proteins, or nucleic acids) can be analyzed and the lateral resolution that can be obtained.

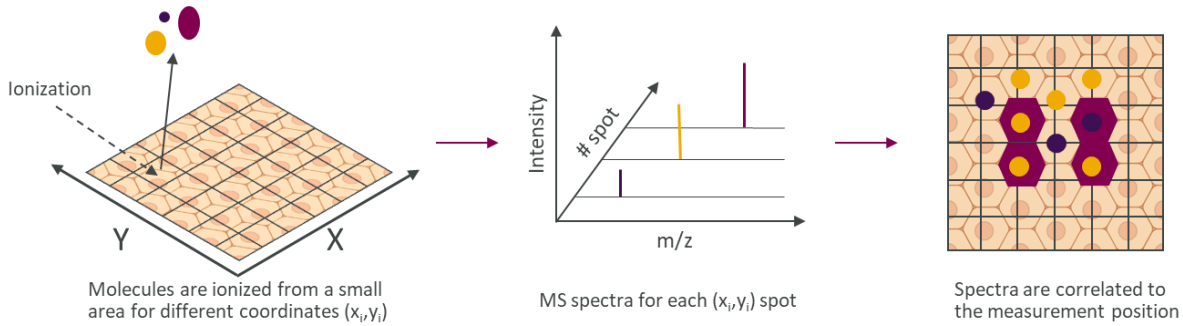

Figure 2. Schematic overview of mass spectrometry imaging principle. The ionization probe is used to raster the sample surface. At each spot along coordinates (x_i, y_i) a mass spectrum is generated. An image with the pixel resolution of the probe size is reconstructed for each (x_i, y_i) pair to visualize the distribution of ions of interest.

The most widely used MSI methods for biological samples are matrix-assisted laser desorption ionization (MALDI), desorption electrospray ionization (DESI) and secondary ion mass spectrometry (SIMS).[18, 21] Figure 3 recapitulates these MSI techniques characteristics in terms of lateral resolution as well as which molecules can be analyzed. MALDI and DESI are by far the most common MSI techniques that have been applied in pharmaceutical research. Due to the high fragmentation and expensive instrumentation, SIMS is not commonly used for pharmaceutical investigations yet.

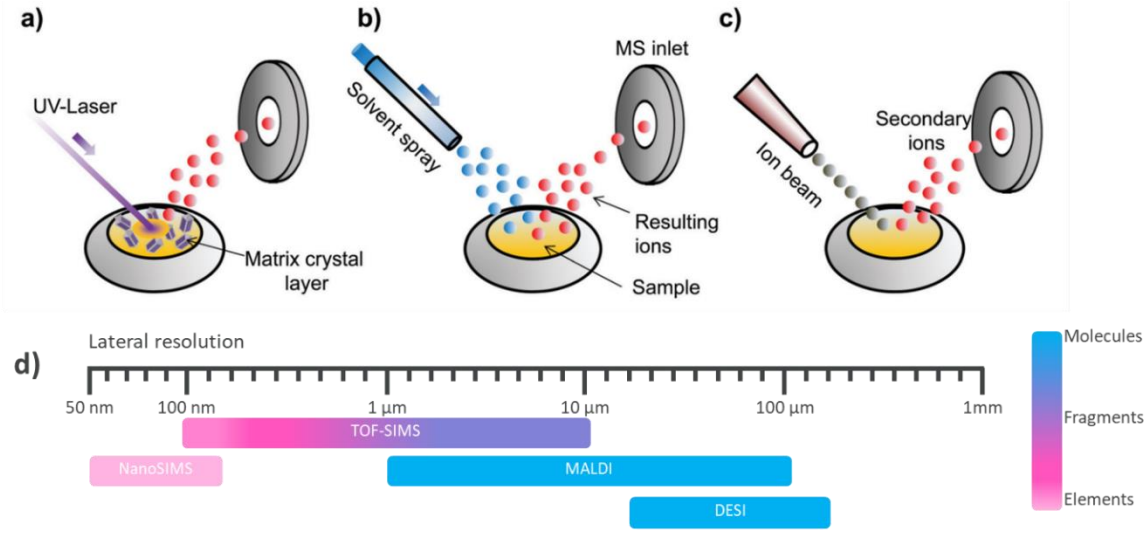

Figure 3. Overview of the different MSI techniques. (a) MALDI-MSI ionization is performed by a laser irradiating the sample, and efficient ionization is obtained by deposition of a UV-absorbing matrix on the sample surface. (b) In DESI-MSI a spray of ionized solvent is directed towards the sample surface for desorption. (c) SIMS imaging, like TOF-SIMS and NanoSIMS, uses a primary ion beam to locally desorb the sample surface. While MALDI and SIMS operate under vacuum, DESI ionization is performed at ambient conditions. (d) Difference in term of lateral resolution and type of ions obtained by the different MSI techniques are also reported. Adapted from Vaysse *et al.*, 2017 [22] and Wang *et al.*, 2020 [33].

MALDI was introduced for biological sample analysis in the 1990s.[34] and is widely used to study large biomolecules like proteins and peptides. MALDI is a relatively simple technique where the ionization is performed by a laser irradiating the sample, and efficient ionization is obtained by deposition of a UV-absorbing small organic molecule, called a matrix, on the sample surface (Figure 3a). A desorption/ionization process follows the irradiation. Typically, MALDI-MSI is considered as a soft ionization technique inducing low ion fragmentation allowing intact molecules to be analyzed. Several matrices have been developed to allow the analysis of a wide range of analytes, from small molecules to proteins. However, one limitation of MALDI-MSI is the ions of matrix generated which may interfere with the detection of analyte ions and this could favor specific analytes and not others.[35] The application of the matrix can also lead to some degree of redistribution. Several groups have worked in this space to find solutions to these pitfalls.[22, 36] This highlights that the technique is relatively sensitive to sample preparation. Historically, MALDI-MSI was coupled to a time of flight (TOF) mass analyzer. However, new and more performant mass analyzers are increasingly replacing the TOF system, like quadrupole ion trap-TOF, Fourier transform ion cyclotron resonance, or Orbitrap as they provide better mass resolution and mass accuracy than the original linear MALDI-TOF instrument. More performant MALDI sources have also been developed to increase sensitivity,

ionization efficiency and lateral resolution.[37] In general, MALDI-MSI provides a spatial resolution of 20 to 50 µm, and 1 to 5 µm with the most sophisticated laser systems.[30, 33] Atmospheric pressure MALDI sources (AP-MALDI) are also available facilitating association with any type of mass analyzer.[38]

DESI was introduced in 2004 as a new ambient ionization technique allowing rapid sample analysis as less sample preparation is required (no matrix or resin embedding needed).[39-42] Ionization is performed by directing electrosprayed charged droplets of solvent onto the sample surface creating secondary charged droplets that contain the desorbed analytes (Figure 3b). The rapid evaporation of the droplets reduces the surface area without reducing the surface charge which results in a columbic explosion effectively ejecting intact molecular ions with single or multiple charges. In DESI, the spraying solution can be selectively changed to ionize a particular molecule of interest. Similar to MALDI, DESI enables the detection of a wide range of analytes from small molecules, lipids to proteins. Like AP-MALDI, DESI is a versatile ambient source that can be combined with any mass analyzer. New sprayer designs have improved the lateral resolution and the sensitivity, however the main limitation of DESI-MSI is the ≈30 to 200 µm achievable lateral resolution limiting its application for cellular resolution imaging.[30, 43] A more compact method, nanospray desorption electrospray ionization (nanoDESI), has also been developed where charged droplets are generated between two capillaries that create a liquid micro-junction at the surface of the sample instead of producing charged droplets via a solvent spray.[42, 44]

Although SIMS was the first ionization technique used for MSI more than 50 years ago [31, 45], its usage in biological research was rather limited and focused mainly on surface and elemental analysis of material. Nowadays, SIMS is used for molecular imaging with subcellular lateral resolution, bringing MSI from the tissue level to the organelle scale.[22, 43] Traditionally, SIMS instruments are divided in two groups based on whether the primary ion beam (Cs^+, Bi_n^+, C_{60}^+,Ar_{4000}^+,etc…) is impacting the sample surface by pulses (as in static TOF-SIMS) or continuously (as in dynamic SIMS). Note that some TOF-SIMS instruments, like the J105, operate in a continuous primary ion beam mode while pulsing the secondary ion beam instead, making it more advantageous for biological samples analysis. For both static and dynamic categories [46], the SIMS ionization process involves bombarding the sample surface with a focused high energy primary ion beam (Figure 3c). When the primary ions collide with the sample surface, the top few atomic layers of the sample are sputtered away in a plume of particles made of electrons, neutral particles and atomic or cluster ions. In general, ionized particles represent less than 5% of the particles released from the sample. Static SIMS utilizes a low intensity primary ion beam which only removes a few layers of the surface and generates larger mass fragments allowing molecular information to be acquired. The name static SIMS comes from the idea that this mode does not "change" the surface under analysis.[46-49] Theoretically this is done by keeping the ion dose below the so-called static limit. In practice this is below 10^{13} at./cm^2. Thus, an ion dose of $\leq 10^{13}$ ions/cm^2 will only interact with 1% of the surface atoms, leaving the surface virtually unchanged to maintain molecular information. Dynamic SIMS exceeds the static limit which means that during the measurement the surface is gradually being eroded, thus the measurement is dynamic. Therefore, dynamic SIMS not only affords the ability to use a higher primary ion beam dose, resulting in higher secondary ion production which increases sensitivity, but also increases fragmentation, meaning that the molecular information is lost and in general only elemental and isotopic information are

retained. Nanoscale secondary ion mass spectrometry (NanoSIMS) is the latest generation of dynamic SIMS instrument and offers the best lateral resolution down to 50 nm.[30, 33]

1.3. NanoSIMS, MSI at and below the cell level

NanoSIMS is a high-resolution imaging and analytical technique that allows the study of small structures (tens of nanometers) at the subcellular level.[50-52] NanoSIMS is advantageously equipped with two ionization sources (Figure 4), a cesium source and an oxygen source to analyze negatively or positively charged secondary ions, respectively.[46, 49] Note that most biological studies rely on the use of the cesium source that induces better ionization yield than the oxygen source and provides a better lateral resolution (down to 50 nm).

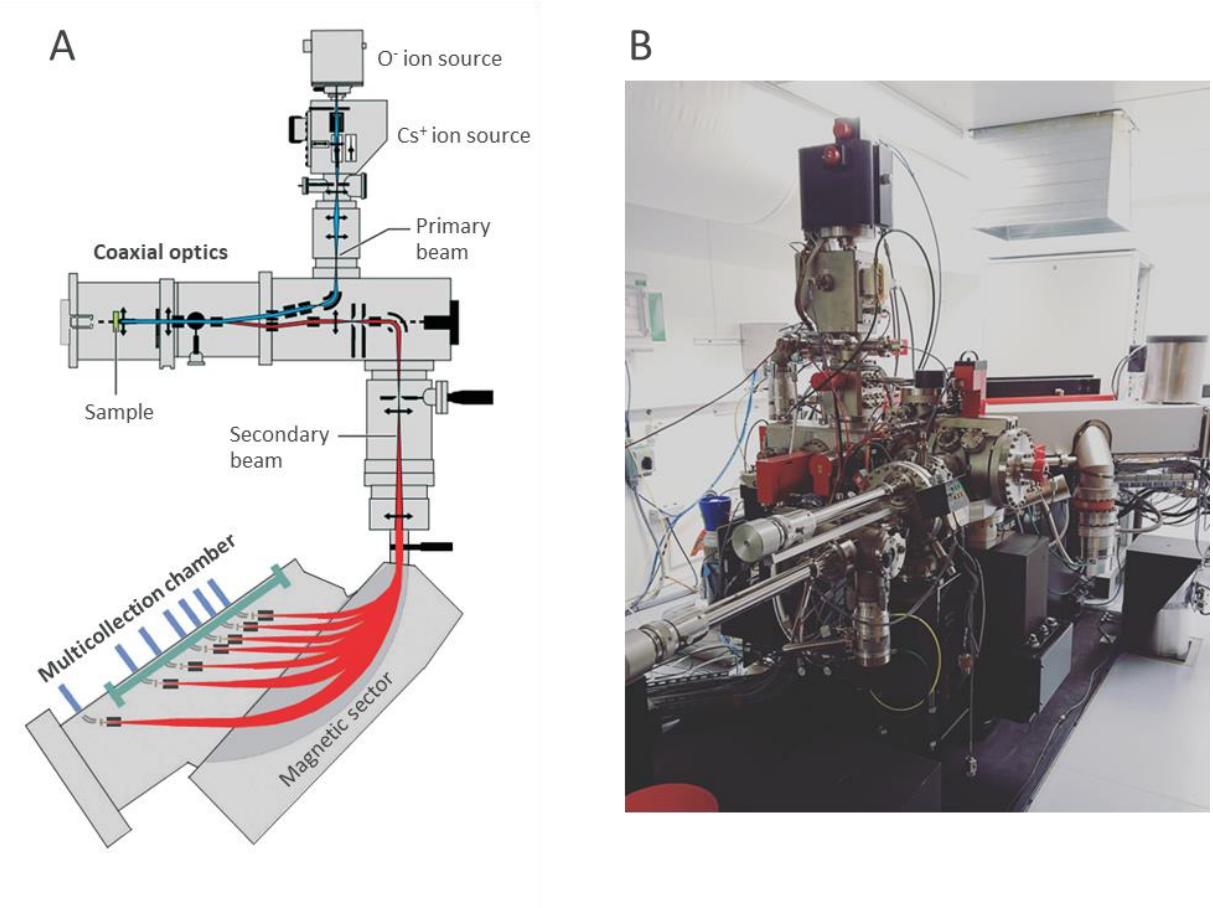

Figure 4. (A) Schematic of the NanoSIMS 50L (adapted from [53] and [51]). The surface of the sample is rastered with a focused primary ion beam. Secondary ions are extracted and guided through a series of ionic lenses and slits to an elctrostatic sector and then to the magnetic sector that separated the ions based on their m/z. Simultaneous detection of up to seven analytes from the same spot on the sample surface is possible. (B) Image of the NanoSIMS 50L instruments housed in the Chemical Imaging Infrastrucuture in Gothenburg.

Apart from the dual source, NanoSIMS instruments are also composed of primary ion optic column to focused and orient the primary ion beam toward the sample, a co-axial column, and a secondary ion optic column that focuses and directs the secondary ions into the mass analyzer (Figure 4).[49] The co-axial configuration of the NanoSIMS is its most significant characteristic that allows considerable reduction in the distance between the sample surface and the primary

ions column producing a tightly focused and intense primary ion beam probe. In the co-axial mode, the same ion optic system is used to both focus the primary ion beam and collect the secondary ions. It is therefore implicit that primary and secondary ions must be of opposite polarity as the secondary ions are extracted via the same diaphragm as the primary ions.

Emitted secondary ions are accelerated through an extraction lens and guided through the secondary ion column via a series of ionic lenses and slits to the entrance of first an electrostatic sector and then a magnetic sector mass analyzer.[48, 49] This combination creates a double focusing mass analyzer that provides a high and continuous transmission along the selected mass range and achieves a high mass resolution. The electrostatic sector separates the secondary ions according to their kinetic energy independently of their m/z ratio. An energy slit at the exit of that analyzer allows the selection of ions in a selected energy range. The magnetic sector deflects the ions via a magnetic field which curve the path of the ions based on their m/z ratio. Ions of the same nominal m/z are then selected and directed in the exit slit of the magnetic sector to an electron multiplier for imaging purposes.[48] Thus, simultaneous detection of up to seven analytes from the same spot on the sample surface is possible. This represents a large improvement compared to older versions of dynamic SIMS equipped with a single detector, although it does not rival with the TOF-SIMS capacity to collect hundreds of m/z values for each analyzed spot.

The whole NanoSIMS system is maintained under ultra-high vacuum to reduce potential collision with gas particles which would drastically affect the transmission efficiency of the secondary ions. However, due to the high fragmentation that occurs during SIMS ionization, only elements and small ions related to the compound of interest can be analyzed. Thus, NanoSIMS analysis requires a targeted labeling-strategy [46] with isotopes, halogens or metals. The mass resolution is sufficiently high to distinguish species of similar molecular weight like $^{13}C^-$ and $^{13}C^1H^-$ or isotopes ($^{32}S^-$, $^{33}S^-$ and $^{34}S^-$ for example).[47-49] NanoSIMS applications in biology include studying the distribution of nutrients and signaling molecules within cells, studying cellular processes such as cell division and cell migration, and determining the cellular localization of proteins and nucleic acids. Importantly, NanoSIMS have had significant success for exploring the distribution of different drugs like cisplatin, amiodarone and more recently oligonucleotide therapeutics.[54-56]

To enhance the information obtained at the nanometer scale, NanoSIMS can be correlated with electron microscopy (EM) techniques such as transmission electron microscopy (TEM) and scanning electron microscopy (SEM).[46, 57] In biological studies, whereas NanoSIMS provides chemical information to determine the distribution of specific elements or isotopes within the sample, EM provides ultrastructural details gaining morphological information and allowing identification of subcellular structures like nucleus and mitochondria.

1.4. Quantitative MSI: Where and how much?

If at its beginning MSI was just a colorful description of molecular distribution, it is now a robust technique that allows simultaneous extraction of qualitative spatial distribution information and the quantitative abundance of a compound. Absolute quantification is needed to ascertain that a drug is reaching its target tissue and intracellular target at sufficient concentration to elicit the desired therapeutic effect. In practice, the quantification aspect remains challenging due to the complex nature of biological samples that impacts the ionization

efficiency and can induce ion suppression linked to matrix effects and the degree of this suppression varies greatly between various tissue and cell types.

Therefore, accurate quantification by MSI (qMSI) is required and several approaches have been developed. An important step for qMSI is to first account for ion suppression, matrix effects, and variations in tissue morphology. These are all compensated for by normalizing drug or metabolite ion signal against an internal standard that is a stable-labeled version of the analyte or a similar compound.[29] Then, for absolute qMSI a calibration standard or set of calibration standards deposited on a control sample or prepared in a matrix of similar chemical composition as the biological sample are analyzed alongside investigational samples.[29] The ion intensities from the sample are correlated to the ion intensities of the standards to quantify the analyte(s) of interest. This also applies to absolute quantification by NanoSIMS.[58]

Chapter II. Antisense oligonucleotides (ASOs).

2.1. Broad overview of oligonucleotide therapeutics

In the 1970s, Zamecnik and Stephenson described the use of short synthetic sequences of nucleic acids to modulate the expression of specific genes.[59] Since then, oligonucleotide therapeutics (ONTs), have arisen as a promising class of drugs for the treatment of various diseases.[60-62] Different types of ONTs with specific modes of action (Figure 5) have been developed for therapeutic use, such as antisense oligonucleotides (ASOs), small interfering RNAs (siRNA), and aptamers.[63-69] ONTs also have potential as vaccines, particularly for viral infections.[63, 64]

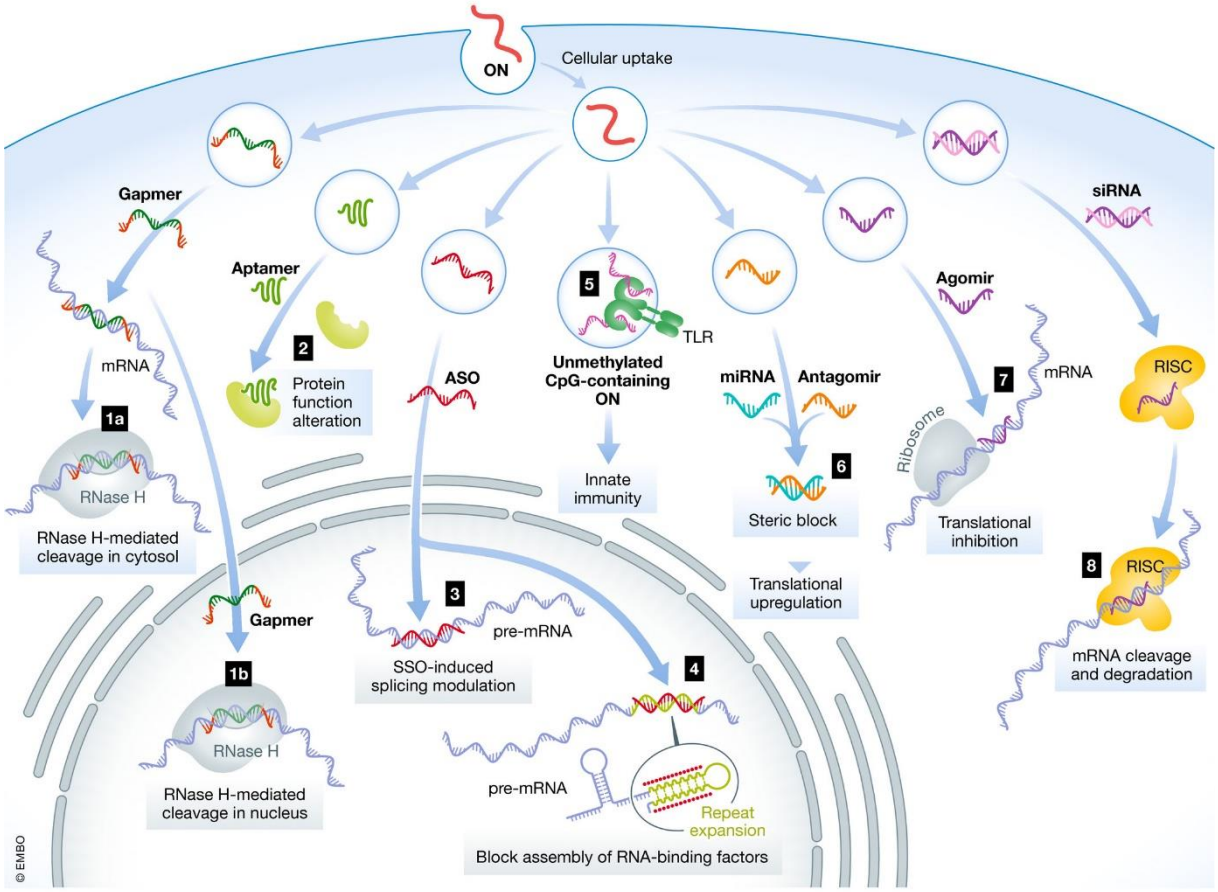

Figure 5. Representative mechanisms of action and intracellular localisation for (1) gapmer and mRNA degradation in the cytosol (1a) and/or the nucleus (1b), (2) aptamer, (3) nuclear steric blockage for splice switching, (4) blocking the assembly of RNA-binding factors, (5) Toll Like Receptor (TLR) activation of innate immunity, (6) miRNA and antagomir as steric blocks for translational upregulation, (7) agomir for translational inhibition, and (8) siRNA loading in the RISC complex for mRNA cleavage. Reproduced with permission from Hammond *et al.*, 2021.

Even if approaches to target RNA structure with small molecules are being investigated [70-73], a large portion of ONTs targets are still not reachable with traditional small-molecule drugs.[61, 74, 75] The dogma is that small molecules need to bind to an active site or an allosteric site with high occupancy on the target to affect function based on the 3D conformation of the target. In practice, this means that a large library of compounds has to be synthesized and screened for biological activity to develop a small molecule into a drug. Therefore, the major

advantage of ONTs is their specificity as they are designed to be complementary to specific messenger RNAs (mRNAs) or non-coding RNA (ncRNAs) through Watson-Crick base-pairing. In principle, this means that ONTs can be rapidly designed against any genetic target contrary to small molecules.

Currently, several ONTs have already been approved by regulators for clinical use and many more are currently in late-stage clinical trials.[61, 62, 66, 67] For example, ASOs like Eteplirsen and Nusinersen are used in the treatment of Duchenne muscular dystrophy by increasing the production of dystrophin, and spinal muscular atrophy by correcting SMN2 splicing defect, respectively. However, despite their potential, there are still challenges that need to be overcome before these therapeutics can be more widely adopted in the clinic.[67, 76, 77]

ONTs are large, polar and negatively charged molecules which render cell penetration difficult.[76, 77] If they make it into cells, unmodified ONTs are then susceptible to degradation by nucleases.[76] Additionally, another challenge is to deliver ONTs to specific tissues or cells within the body.[76, 78, 79] This can be a particular hurdle to reach the brain, for example, due to little or no ability to cross the blood brain barrier, which makes it necessary to use burdensome routes of administration, such as intracerebroventricular.[67, 76, 80] Finally, endosomal entrapment represents probably the major challenge for ONTs. Such drugs indeed must escape endosomes to reach their intracellular targets else they will be degraded, reducing drug efficacy.[81-83] Several strategies are under development to tackle these different hurdles [66, 67, 78] and will be described below with an emphasis on ASOs as molecules of interest for this thesis.

2.2. Chemical modifications of ASOs

Medicinal chemistry of ONTs is a vast field of research and a great diversity of chemical modifications has been developed and reported in many reviews.[65, 66, 78, 84-87] This chapter will provide a summary of the main chemical modifications that have been incorporated in the ASOs used in this thesis. Namely, phosphorothioate (PS) backbone, locked nucleic acid (LNA), constrained 2'-O ethyl (cEt), pyrimidine methylation and bioconjugation.

Briefly, ASOs are short (usually 12 to 25 nucleotides), single-stranded synthetic nucleic acids designed to modulate gene expression [65] following two major mechanisms (Figures 5 and 6): RNA cleavage or RNA blockage.[66, 85, 88-91] Most ASOs approved by the regulators exert their biological effect via RNases. In particular, gapmer ASOs form heteroduplexes with their RNA target, which serve as a substrate for RNase H enzymes. This ubiquitous RNase H enzyme recognizes and cleaves RNA-DNA heteroduplexes as well as gapmer ASO-RNA duplexes, leading to the degradation of the target RNA.[92] A gapmer ASO is made of central unmodified DNA nucleotides (called the gap) flanked on both sides by 2´-modified RNA nucleotides (called the wings). Another type of ASOs causes translational arrest due to steric hindrance.[91] This type of ASOs does not induce RNases H to cause cleavage but inhibit the interaction between the target RNA and ribosomal subunits. In addition to the non-degrading mechanism, most mRNA undergo complex cellular processing such as alternative splicing to obtain a protein, and such steric-blocking ASOs can be used to correct splicing aberration.[93]

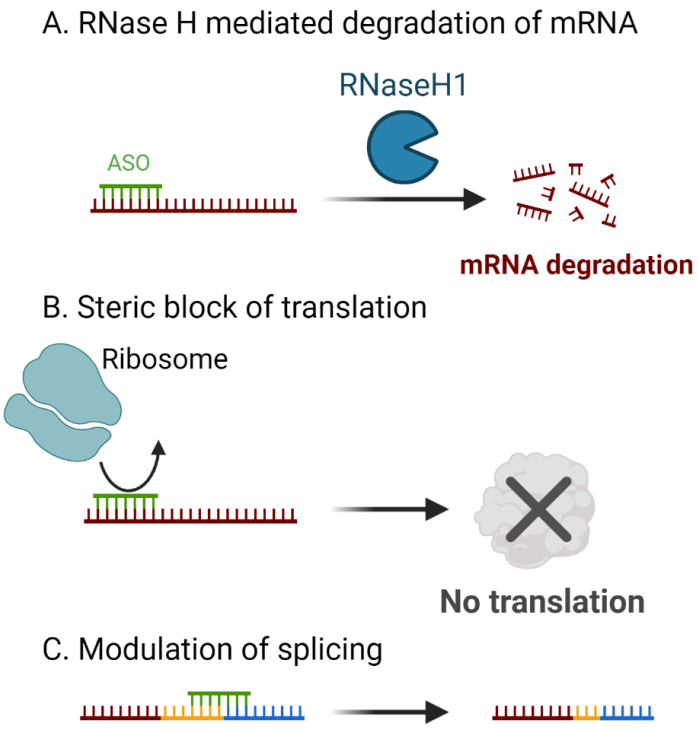

Figure 6. Schematic representation of ASOs mechanisms of action. Some ASOs are designed to elicit RNase H mediated mRNA degredation (A). Other type of ASOs can cause translational arrest by inhibiting the interaction between the target RNA and ribosomal subunits (B). ASOs can also be designed to modulate splice-switiching process (C). Created with BioRender.com.

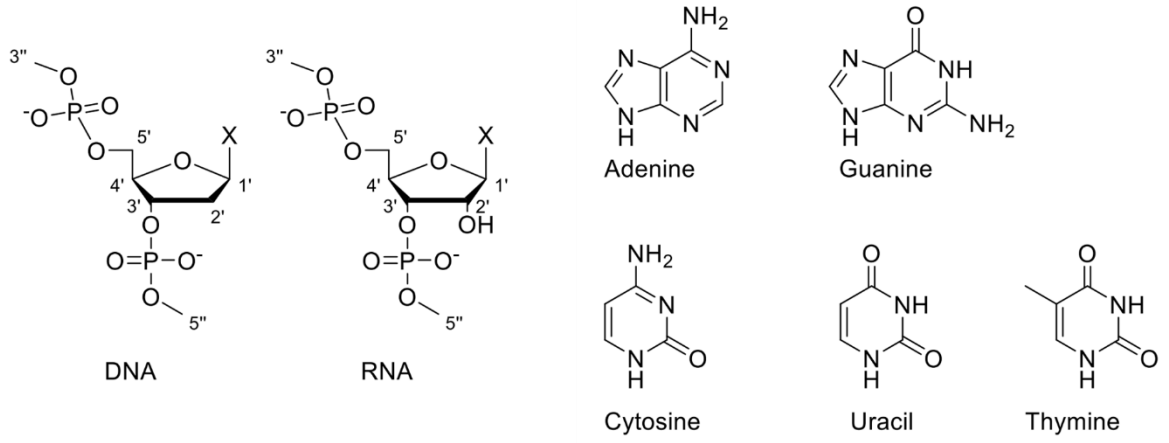

Figure 7. General structure of DNA and RNA of oligonucleotides. X = nucleobase (Adenine, Guanine, Cytosine, Thymine or Uracil).

The first ASOs used were synthetic unmodified deoxyribonucleotides (Figure 7). However, these native ASOs were rapidly cleared from blood circulation due to poor plasma protein binding, reducing tissue distribution and favorizing renal excretion. In addition, these ASOs were highly sensitive to endo- and exo-nucleases and could not permeate plasma membranes. Therefore, it became clear that chemical modifications were required to improve ASO performance by introducing changes in the backbone, nucleobases and sugar moieties (Figure 8).[65-67, 78, 84-87, 94]

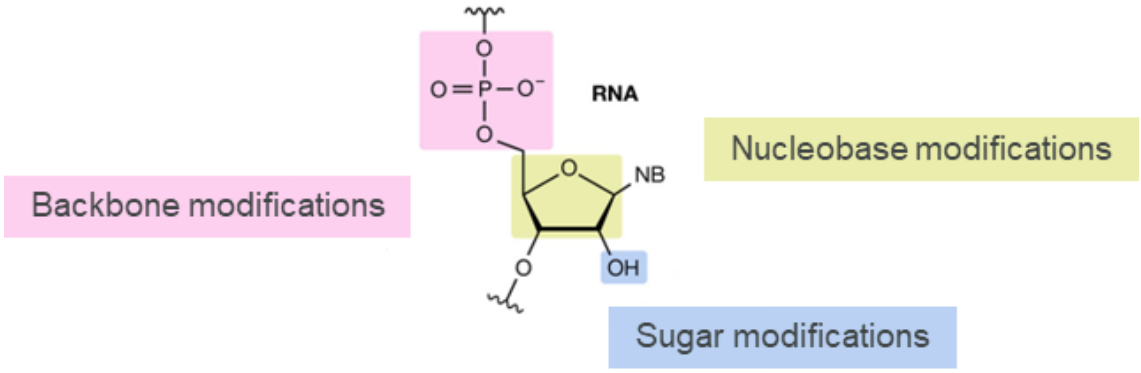

Figure 8. Site of modifications of ASOs. NB: nucleobase. Adapted from Hammond *et al.*, 2021.

The phosphorothioate (PS) linkage, where a non-bridging oxygen atom of the phosphodiester (PO) linkage is replaced by a sulfur atom, is the most widely used modification for therapeutic ASOs (Figure 9).[95] PS-ASOs show increased stability compared to PO-ASOs, as well as plasma protein binding and cellular uptake. The affinity of the PS-ASO with various proteins is also influencing cellular uptake and trafficking thereby affecting PS-ASOs pharmacological effect.[96, 97] Moreover, PS backbone generally does not disrupt RNase H recruitment and activity. Unfortunately, most PS-ASOs show significant toxicity, directly proportional to the number of PS linkages incorporated in the ASO backbone.[76, 98] This toxicity is thought to be mostly linked to non-specific binding of the PS backbone to intracellular proteins. Note that the introduction of a sulfur atom creates a chiral center on the phosphorus atom, and the resulting stereoisomers could exhibit different potency.[99] PS modification also reduces binding affinity to the target RNA, but that limitation can be balanced by incorporating additional modifications (see below).

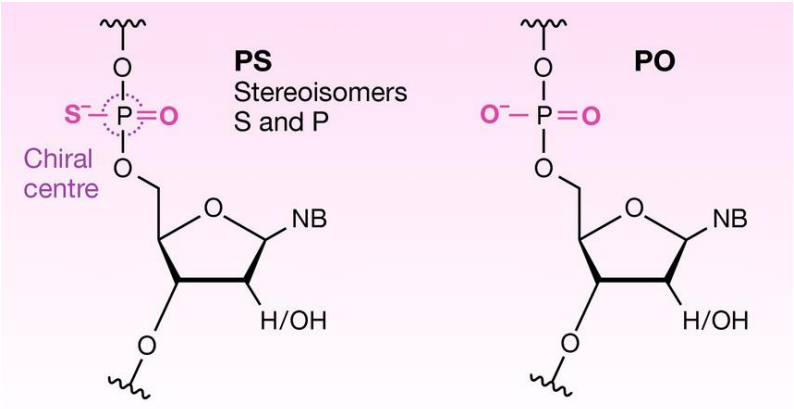

Figure 9. The phosphorothioate (PS) backbone replaces the natural phosphodiester (PO). Here the non-bridging oxigen atom of the internucleotide PO linkage is substituted with a sulfur atom to avoid ASO degradation by nucleases. This substitution results in the generation of a chiral center. Adapted from Hammond *et al.*, 2021.

To improve ASOs and develop them into potent therapeutics, more advanced chemical modifications were introduced. A second-generation of modification occurs at the 2´-position of the ribose entity to further enhance nuclease resistance, reduce toxicity and increase target RNA binding. Importantly, a major disadvantage of this second-generation is their inability to induce RNase H cleavage. For this reason, second-generation ASOs are often designed as

gapmers with a partial or full PS backbone to combine the nuclease resistance and the RNase H recruitment.

More recently, new bridged nucleic acid (BNA) modifications have been developed to further enhance binding affinity by restricting flexibility of the ribose. The most commonly BNAs are locked nucleic acid (LNA) and constrained 2'-O-ethyl (cEt) analogues that are conformationally restricted by a methylene group that bridges the 2´-oxygen atom and 4´-carbon atom of the ribose ring (Figure 10). These BNAs provide nuclease resistance and higher hybridization affinity towards complementary RNA, but still do not activate RNase H and are therefore excluded from the DNA gap. The use of BNAs allows for the synthesis of shorter gapmers leading to enhanced delivery and reduced PS content and therefore reduced immunostimulation and toxicity.

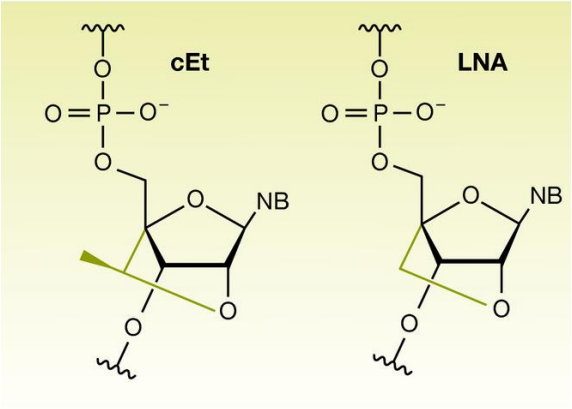

Figure 10. Conformationally constrained nucleobase. cEt: constrained 2'-O-ethyl, LNA: locked nuclei acid. cEt and LNA are constrained by a methyl bridge from the 2´-O and 4´position of the ribose Adapted from Hammond *et al.*, 2021.

It is also possible to modify the nucleobases, for example by methylating pyrimidines at their position 5.[84] This methylation, which is a naturally occurring phenomenon in cells, increases the melting temperature by ~0,5˚C per modification.[100] This stabilizes the ASO-RNA heteroduplex and enhances nuclease resistance and reduces immunostimulation.

Bioconjugation is the last chemical modification to make ASOs more selective drugs, by addressing them to the right cells. The earliest approach was to conjugate ASOs to fatty acids and lipids such as palmitic acid, cholesterol, and α-tocopherol.[101-103] Aptamers and antibodies have also been investigated.[66] As of now, the most successful application already in the clinic, is the conjugation to a *N*-acetylgalactosamine (GalNAc), a ligand for the asialoglycoprotein receptor (ASGPR) that is highly expressed on hepatocyte cell membranes.[104-106] Typically, a triantennary GalNAc structure is used, enhancing ASO potency by 10- to 30-fold in patients compared to unconjugated ASOs.[94, 107] Recently, it was demonstrated that an engineered glucagon like peptide 1 (eGLP1) could also be used to facilitate ASO uptake in pancreatic beta cells by targeting the glucagon like peptide 1 receptor (GLP1R).[108, 109]

It is important to note that the cellular uptake efficiency and trafficking of ASOs can be influenced by several factors, such as chemical modifications of ASOs, the cell type being targeted and the presence of other molecules competing for uptake. Optimization of these key processes are lively ongoing areas of research in the development of ASO therapeutics.

2.3. Cellular uptake and trafficking of ASOs

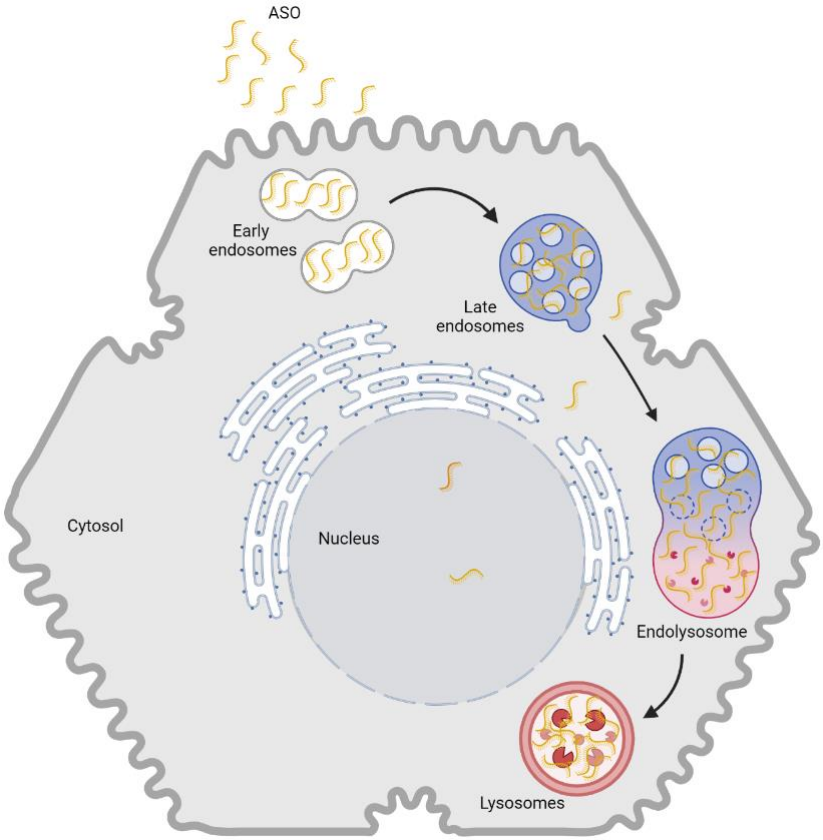

Figure 11. Cellular uptake and trafficking of ASO. The absorption of PS-ASO on cell surface proteins, including the ASGPR receptor for uptake of GalNAc conjugates, induces the internalization of ASO via different endocytosis pathways. Then, internalized ASOs are concentrated in vesicular organelles and traffic from early endosomes to late endosomes and to lysosomes. ASOs must escape the endolysosomal space to reach their target in the cytosol and/or nucleus. Created with BioRender.com.

Investigation of mechanisms of ASO entry into cells has intensified in recent years. Mechanistically, once ASOs reach the cell membrane, whether in their unconjugated or conjugated form, they are internalized by endocytosis and traffic through different intracellular compartments (Figure 11).[80, 81, 110] Endocytosis is a complex process by which cells take in molecules from their environment by forming small vesicles around them. This process can be mediated by clathrin, caveolae, or macropinocytosis. Receptor-mediated endocytosis is also a specialized form of endocytosis that uses specific receptors on the cell membrane to induce uptake of specific molecules. All these processes have been described in the initial uptake of ASOs with different degrees of involvement. Increasing evidence indicates that the initial route of ASO uptake plays an important role on their biological activity. Indeed, even if an ASO is taken up by a cell it does not always elicit a change in mRNA target level or protein expression. This phenomenon is called “non-productive uptake”, while the uptake that leads to a pharmacological effect is termed “productive uptake”.

The intracellular fate of ASOs is determined by the cell endocytic and trafficking machinery. Once ASOs are delivered to the target cell, they need to distribute within the cell and reach their site of action (the cytosol and/or nucleus) at sufficient concentration. Irrespective of the internalization pathway, ASOs are initially delivered to early endosomes (EEs) and trafficked

to late endosomes (LEs), and later to lysosomes where they eventually are degraded (Figure 11). Therefore, to distribute within the cell and reach the target mRNA, ASOs must escape the endosomal compartments. The movement of EEs to lysosomes is a complex and dynamic process mediated by the cytoskeleton, made of microtubules and actin filaments. A plethora of proteins are also involved in the fusion of these different membraned-bound compartments. Thus, intracellular trafficking of ASOs is tightly regulated by a set of proteins, the interactions of which vary in time and space. While it might seem to be a limitation to fully understand ASO subcellular distribution it also opens the door to manipulating their trafficking and potentially enhance their potency.

2.4. Endosomal escape

The mechanism(s) by which ONTs escape into the cytoplasm remains unclear.[82, 83, 111] One hypothesis is that small breaches may appear temporarily and spontaneously on the endosomal lipid bilayer and this will over time allow the ONTs to reach the cytosol. Fusion events occurring between EEs, LEs, and lysosomes may also cause such breaches. Some data also suggest that ONTs may also escape via retro-transport from the Golgi. However, understanding the underlying mechanisms behind endosomal escape would be an important steppingstone to enhance escape and develop more potent ONTs.

Indeed, once internalized, the ASOs are entrapped in endosomes and at some point in time during the subcellular trafficking process it is hypothesized that around 1% escape to the cytosol (Figure 11). The other 99% remains trapped in the endolysosomal space unable to reach their target.[82, 83, 110] Thus, endosomal escape is considered as a critical factor for ASOs to elecit their biological effect also preventing ASO widespread use in the clinic. The escape rate and amount leaked is dependent on the target cell and the chemistry of the ASO.[111, 112]

New strategies aim at enhancing the escape of ASOs to improve their activity, especially for clinical perspectives, by altering/permeabilizing the endosome membrane or changing the endosomal pH using small molecules. In a recent study, chloroquine, a well-known drug used to induce endolysosomal compartment rupture, was used to improve ASO activity and suggested that the release of oligonucleotides to the cytosol was likely related to LEs.[113] Although displaying great potency *in vitro*, chloroquine needs to be used at high micromolar concentration (40 to 100 μM) to induce leakage and is not viable for therapeutic purposes. Juliano *et al.* have identified several other compounds that can induce escape from LEs at more reasonable concentrations (5-30 μM).[82] To improve the therapeutic window between potency and toxicity, Bost *et al.* recently identified a new class of compounds inducing endosomal escape at concentrations below 5 μM.[114]

2.5. Different methods to assess ASOs uptake and distribution

Figure 12 shows different assays to measure the functionality of an ASO or to assess ASO total cellular uptake. In general, to determine the potency of an ASO, the target mRNA and/or protein levels are assessed by reverse-transcriptase quantitative polymerase chain reaction (RT-qPCR) and Western Blot, respectively. This can be related to the productive uptake of an ASO as only the ASOs that successfully reach their target lead to ASO activity.[115-117] A set of fluorescence-based techniques can be used to assess the relative cellular amount of ASOs and

their subcellular localization.[115-120] This also enables co-localization studies with various proteins involved in the endocytosis and trafficking pathway of ASOs.[121-123] However, addition of a dye can modify the uptake and trafficking of the ASOs due to interaction with proteins at the cell membrane.[11, 12, 124] Immunofluorescence assays can bypass the dye potential alteration of the ASO uptake, but this method requires that an antibody designed against the ASO is available to measure the relative amount of internalized ASOs.[125, 126] Liquid chromatography coupled to mass spectrometry (LC-MS) and enzyme-linked immunosorbent assay (ELISA) can also, via calibration standards, accurately quantify ASO total cellular uptake in cells or tissue homogenates but the localization aspect is lost.[115, 127, 128] Associating LC-MS or ELISA with subcellular fractionation can offer information about ASO subcellular distribution but in practice this method is challenging and burdensome.[115, 129] Additionally, the aforementioned methods do not offer much direct insight into precise measurement of total uptake and the distribution of ASOs.

There is a need for a sensitive detection method to measure the total cellular uptake of ASOs and to determine their localization within cells to distinguish how much ASOs are reaching the cytosol and/or nucleus (productive uptake) or how much remains trapped in endolysosomal compartments (non-productive uptake). Therefore, in this thesis I decided to build on the analytical performances of the NanoSIMS both to measure ASO cellular uptake and to investigate their subcellular distribution and trafficking.

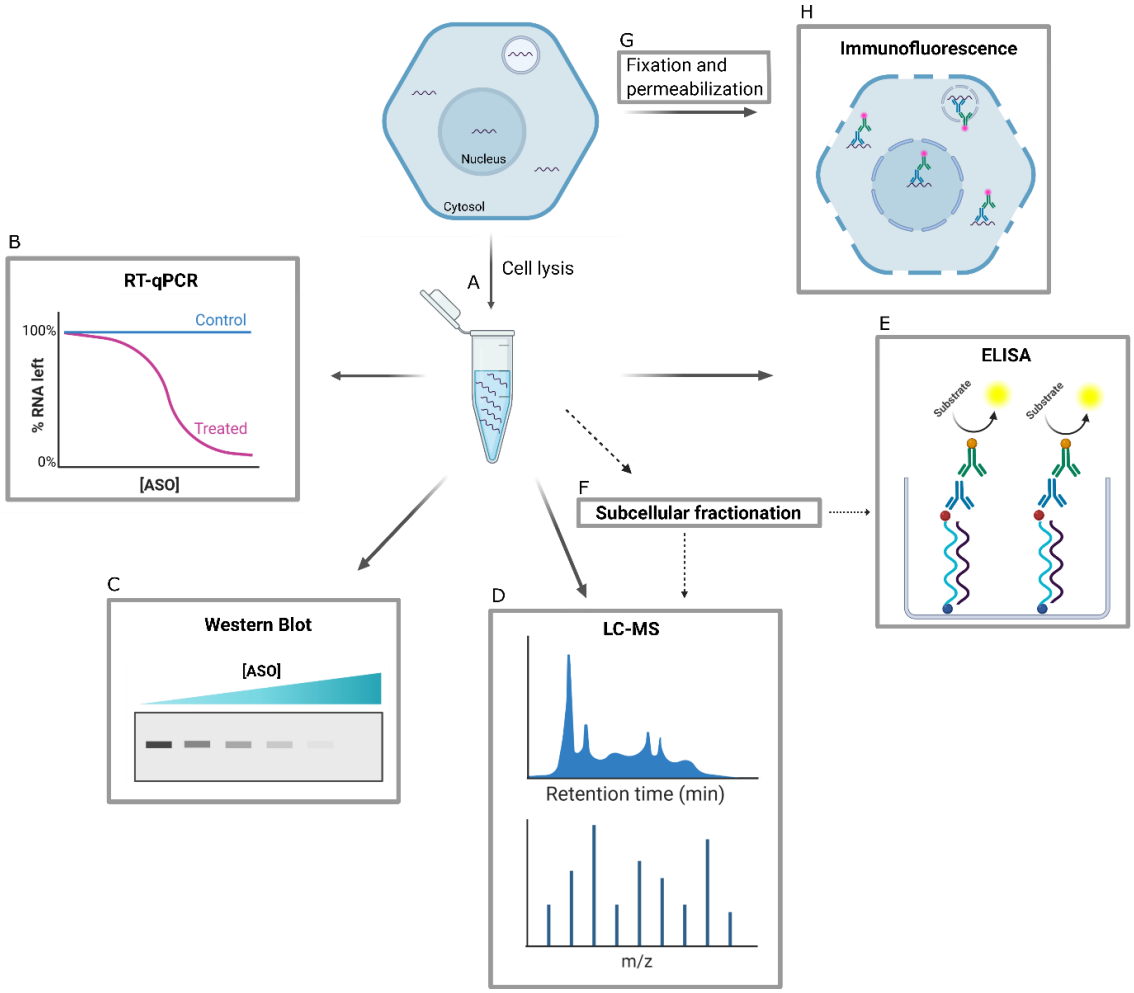

Figure 12. Summary of different assays to measure functional activity of ASO or to measure total cellular uptake. After ASO incubation, cells are lysed in the appropriate buffer (A). Functional activity can be assessed by measuring mRNA knockdown (B) or by detection the protein of interest by Western blot (C). After homogenization and lysis of cells or tissues, the concentration of unlabeled ASO can be measured by LC-MS (D) or ELISA (E). A subcellular fractionation step can be performed on the lysate (F) before performing LC-MS or ELISA assays to gain insight on ASO subcellular distribution. For immunofluorescence of an unlabeled ASO, cells or tissues are fixed, permeabilized (G) and incubated with antibodies to selectively recognize the ASO (H).

Chapter III. Research aims.

One critical requirement, when it comes to the development of a therapeutic molecule, is to understand the subcellular distribution and concentration of the drug. For ASOs, it is even more important to assess this at the cellular and subcellular level due to their mode of action within the cell (Figure 4). A large effort has been undertaken by several research groups to gain mechanistic understanding of how ASOs (and other ONTs) are internalized by cells and escape the endosomal space as that largely influences ASOs activity. Nonetheless, it is still a challenge to precisely assess the internalization and endosomal escape of ASOs and there is a need for sensitive detection methods to measure the total cellular uptake of ASOs and to determine their localization within the cell. Therefore, the overall purpose of this thesis project was to establish a NanoSIMS absolute quantification method to measure the intracellular concentration of ASOs and correlate it to their localization within the cell and their potency.

The specific aims were:

- To map the subcellular distribution of ASOs by correlative electron microscopy and NanoSIMS (Paper I, II, III & IV).
- To provide ASO intracellular concentrations by expanding the NanoSIMS quantification method developed by Thomen *et al.* for ^{13}C labeled drugs to other isotopes and elements (Paper I & II).
- To investigate the role of ligand-conjugation on ASO cellular uptake compared to an unconjugated ASO. (Paper II & IV)
- To study the effect of small molecule drugs on ASO trafficking (Paper III).
- To correlate ASO intracellular concentration and number of entrapped ASO molecules with target RNA levels (Paper II & III).

Chapter IV. Development of an absolute quantitative NanoSIMS approach to probe ASOs intracellular concentrations.

ASOs represent ideal compounds for NanoSIMS analysis as they are fully synthetic molecules, thus it is possible to introduce any isotopic or elemental labels in their sequence.

4.1. The first step to absolute quantification by NanoSIMS: the ^{13}C approach

Recently, Thomen *et al.* presented a new NanoSIMS approach to directly map the distribution of drug labeled with a non-toxic rare stable-isotope and to determine its absolute concentration at the organelle level.[58] This method has been successfully applied in different projects.[130-132] This strategy is built on the fact that the carbon content of the Agar 100 resin (54 M) is homogeneously distributed and matches extremely well with the carbon content of the embedded cell. Thus, it is straightforward to convert the ^{13}C enrichments (eq. 1) linked to the labeled drug into concentrations where the carbon background is used as a standard. This is then quantified by using eq. 1 and 2.

$$\delta^{13}C\ (‰) = \frac{{}^{13}C^{-} / {}^{12}C^{-}}{VPBD} \times 1000 - 1000 \quad (1)$$

$$[^{13}C.drug]\ (\text{in M}) = \frac{(\delta^{13}C_{ROI} - \delta^{13}C_{control})}{1000} \times \frac{VPDB \times 54M}{N^{13}C} \quad (2)$$

Here, $\delta^{13}C_{ROI}$ is the isotopic carbon enrichment in per mille (‰) in different regions of interest (ROIs) of the treated sample and $\delta^{13}C_{control}$ is the enrichment in a blank resin. Both are calculated relative to the Vienna Pee Dee Belemite reference material (VPDB = 0.0112372, eq.2). $N^{13}C$ corresponds to the number of labels incorporated in the drug.

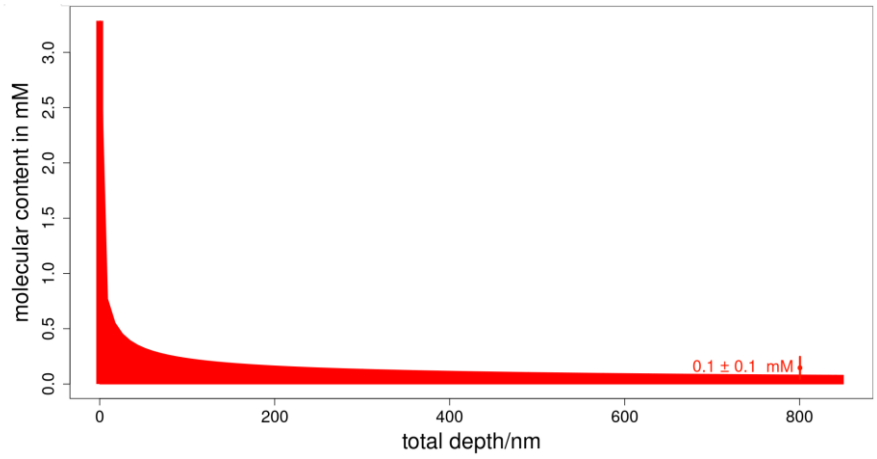

Figure 13. Screenshot of the ^{13}C-labeled content calculator (http://molcat.it.gu.se/) used to predict the uncertainty in concentration by probing 800 nm depth of the material for an ASO labeled with 20 x ^{13}C in a 200 nm organelle. The red area represents the detection limit with respect to the selected parameters.

This approach is also a substantial steppingstone to precisely quantify ASO uptake and correlate it to their subcellular distribution. However, using the web application (http://molcat.it.gu.se/) provided by Thomen *et al*, it was determined that the ^{13}C labeling was

not the most appropriate strategy for ASO detection and absolute quantification as ^{13}C quantification suffers from a low limit of detection.

Indeed, it was estimated that to detect a 100 µM enrichment of an ASO labeled with 20 x ^{13}C in a structure of 200 nm diameter, like an endosome, a total sample depth of at least 800 nm must be analyzed (Figure 13). This represents a long (around 7 h) and unreasonable analysis time. For practical analysis in a pharmaceutical context the time should be below 2 h. Moreover, the predicted uncertainty of the measurement with ^{13}C was determined to be ≈ 100 µM, which was not sufficient to accurately assess the amount of ASOs in a cell. Finally, this measurement is technically impossible given the fact that a roughly spherical 200 nm endosome will not extend into the 800 nm depth required. Incorporating more than 20 x ^{13}C could lead to better analytical performance but that will come with a high cost of production of the ASO.

This led to the use of other labeling strategies that will be described in the next sections of this chapter.

4.2. Relative sensitivity factor to expand the ^{13}C quantification to rare atomic elements

Contrary to ^{13}C, the abundance of other rare isotopic or atomic labels in the resin is not known or is below the detection limit of elemental analysis.[58] Therefore, to quantify these other rare isotopic or atomic labels it was necessary to rely on the use of a relative sensitivity factor (RSF) generated by drawing a calibration curve based on external standards.[133-135] Here, building on the equivalent carbon concentration between the biological sample and the resin, the standards can be prepared in a similar fashion as standards for other quantitative assays, i.e., by spiking a known concentration of the analyte label into the Agar 100 resin. Using an RSF also accounts for variables such as tuning or instrument response and therefore the standards can be used on other NanoSIMS instruments.

4.2.1. Moving from quantification based on ^{13}C to ^{127}I (Paper I)

I first sought to obtain a RSF for an ^{127}I halogen label due to its low natural abundance in the biological sample and the resin as well as its high ion yield. Here, we used amiodarone which endogenously contains two iodide atoms and has already been studied by NanoSIMS [55]. Furthermore, amiodarone can also be labeled with ^{13}C which allows to verify the amiodarone concentration by comparing the values obtained with the ^{13}C approach or calculated based on the iodide RSF. Therefore, the resin was spiked with the duo-labeled amiodarone.

Based on the duo-labeled amiodarone standards (Figure 14), the RSF_{127I} was between 2.98 $x10^{-2}$ mM^{-1} and 3.54 $x10^{-2}$ mM^{-1} for two iodide atoms. This represents less than 20% variation which is considered acceptable for inter-assay measurement. Indeed, these RSFs were obtained from two sets of standards measured during different NanoSIMS experiments, thus some variations due to the tuning were expected. However, this made it necessary to analyze at least one standard per NanoSIMS experiment to ensure the consistency of the measurements. As expected, since both labels originate from the same molecule, the ^{13}C and ^{127}I concentrations matched up, validating the ^{127}I quantification approach.

An adaptation of the formula presented by Thomen *et al.* had to be made to quantify ^{127}I-labeled drugs (eq. 3). Here, the $^{127}I^-$ data are first corrected by the homogeneous $^{13}C^{12}C^-$ level and then corrected by the $^{127}I^-/^{13}C^{12}C^-$ signal of a control cell to account for the background signal. Then, similar to the ^{13}C quantification, data are normalized by the number of labels

(N^{127I}). Thus, only the excess in ^{127}I-labeled drug is obtained and can be calculated as shown in eq. 3 by applying the RSF_{127I}.

$$[^{127}I.drug] = \left(\frac{^{127}I^-}{^{13}C^{12}C^-}\ sample - \frac{^{127}I^-}{^{13}C^{12}C^-}\ control \right) \times \frac{1}{N^{127}I} \times \frac{1}{RSF_{127I}} \quad (3)$$

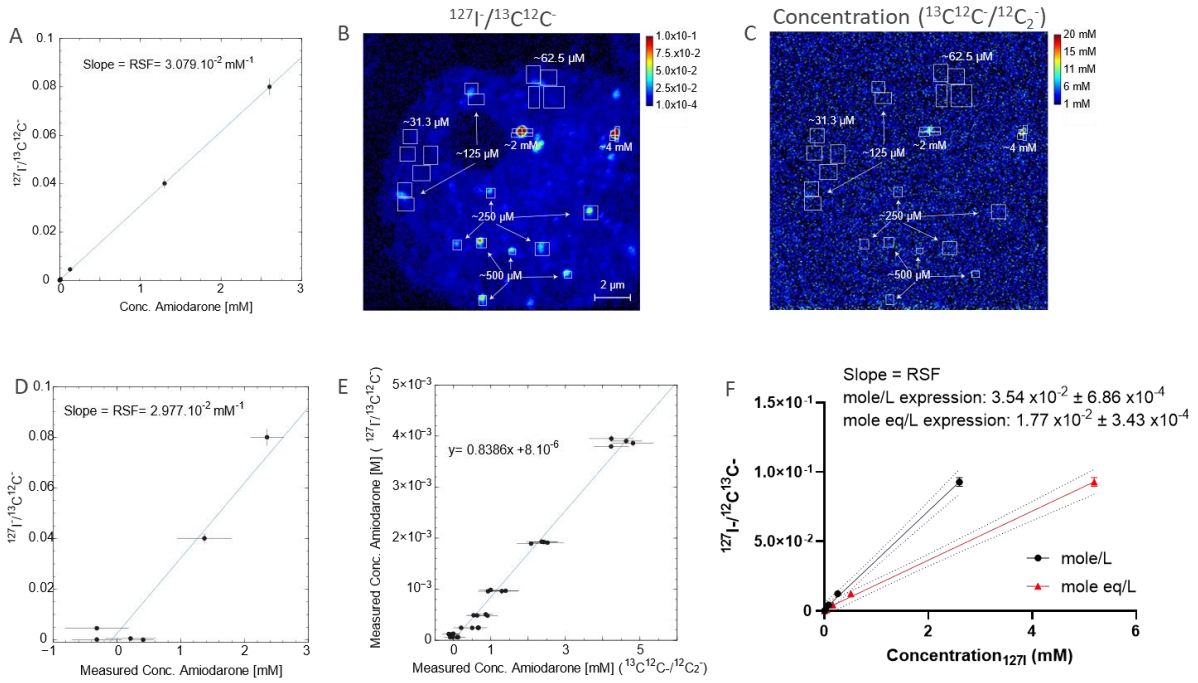

Figure 14. (A) $^{127}I^-/^{13}C^{12}C^-$ calibration curve based on standards spiked with ^{13}C labeled amiodarone. A RSF for ^{127}I of 3.08 x10^{-2} mM^{-1} was obtained. (B, C and D) On cell calibration of ^{13}C-labeled amiodarone. (B) $^{127}I^-/^{13}C^{12}C^-$ ratio image of an NR8383 macrophage treated with ^{13}C labeled amiodarone (2.3 µM for 72 h). The $^{127}I^-/^{13}C^{12}C^-$ ratios are indicated by the color bar. Then, the corresponding $^{13}C^{12}C^-/^{12}C_2^-$ ratio image of the same NR8383 macrophage was converted into a concentration image (C) using the ^{13}C quantification method of Thomen *et al.* The concentration image was scaled from 1 mM to 20 mM as indicated by the color bar. 28 ROIs were selected across the cell. (D) A calibration curve was obtained by plotting the $^{127}I^-/^{13}C^{12}C^-$ ratios of these 28 ROIs against the ^{13}C related concentration using the Thomen *et al.* method (RSF of 2.98 x10^{-2} mM^{-1}). (E) Linear regression comparing the concentration of the ^{13}C-labeled amiodarone using the Thomen *et al.* method and the RSF for iodide (3.08 x10^{-2} mM^{-1}) from the 28 ROIs ranging from 4 mM to 31.3 µM across the NR 8383 macrophage treated with ^{13}C labeled amiodarone. (F) Another calibration curve for iodide was obtained based on another batch of standards spiked with amiodarone. A RSF of 3.54 x10^{-2} mM^{-1} was obtained. However, all the RSF values mentioned here were based on the concentration of the amiodarone molecule (mole/L), and did not account for the two iodide atoms of the molecule. Therefore, the concentration of ^{127}I (mole equivalent expression) is twice the concentration of amiodarone.

Based on the RSF, a limit of detection (LOD) and limit of quantification (LOQ) were determined as follow: LOD = (3.3 x $\sigma_{blankAgar100}$)/RSF and LOQ = (10 x $\sigma_{blankAgar100}$)/RSF, where $\sigma_{blankAgar100}$ is the calculated standard deviation of $^{127}I^-/^{13}C^{12}C^-$ ratios measured on a blank resin and the RSF is expressed in mM^{-1}. The LOD_{127I} and LOQ_{127I} were estimated to be ≈ 2 µM and ≈ 5 µM, respectively, suggesting that smaller ASO enrichments can be detected with the iodide labeling strategy.

4.2.2. Quantification via ^{81}Br (Paper II)

A bromide halogen label has also successfully been used to image nucleotides by SIMS.[56, 136, 137] Therefore, I also decided to determine a RSF for that atom to further expand the NanoSIMS quantification toolbox. This will be helpful to compare different labeled molecules head-to-head, as presented in Nguyen *et al.* for example.[130]

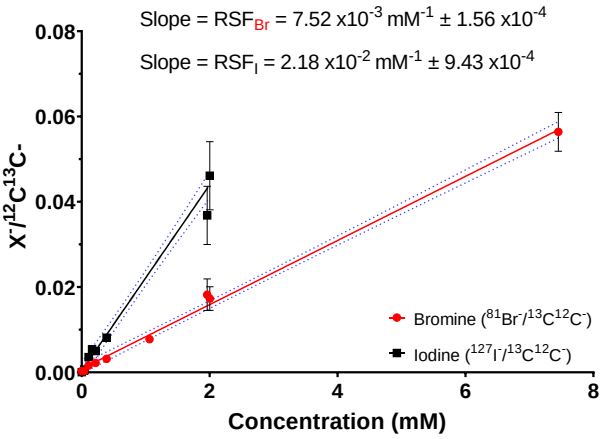

Figure 15. Iodide and bromide calibration curves. To obtain external standards different amounts of 1-bromo-4-iodobenzene were spiked in either Agar 100 resin or EpoxyCure2. No differences in $^{81}Br^-/^{13}C^{12}C^-$ or $^{127}I^-/^{13}C^{12}C^-$ ratios were observed between the two resins tested. Thus, all the standards were used to draw the standard curves. To obtain the RSF for ^{81}Br and ^{127}I, the $^{81}Br^-/^{13}C^{12}C^-$ or $^{127}I^-/^{13}C^{12}C^-$ ratios, expressed as $X^-/^{13}C^{12}C^-$ on the graph, were plotted against the concentrations of 1-bromo-4-iodobenzene. Dotted lines represent 95% confidence interval.

I developed new iodide and bromide standards by spiking the Agar 100 resin with different amounts of 1-bromo-4-iodobenzene (Figure 15). Similar to the duo-labeled amiodarone, it was determined that the previously published calibration curve for iodide (paper I), would serve as an internal reference to validate the newly obtained RSF for bromide. Some standards were also prepared in EpoxyCure2 to determine if the approach could be applied to other resins for which the carbon content was not yet determined by elemental analysis. No differences in $^{81}Br^-/^{13}C^{12}C^-$ or $^{127}I^-/^{13}C^{12}C^-$ ratios were observed between the two resins tested and it was deemed acceptable to use all the standards for the standard curves. This also allows exclusion of potential matrix effects.

To be comparable to the bromide quantification, which was based on one atom of bromide in the 1-bromo-4-iodobenzene molecule, the RSF_{127I} had to be expressed as millimole equivalent per liter instead of mole per liter. Hence, the RSF for iodide was 1.77 x10^{-2} mM^{-1} for one iodide atom while it was of 3.54 x10^{-2} mM^{-1} for two iodide labels (Figure 14F). Thus, the millimole equivalent per liter expression is preferred for all standards to readily compare the several labels used in this thesis indifferently of the number of labels.

The previously published iodide calibration curve was validated. Indeed, the RSF based on the 1-bromo-4-iodobenzene molecule for ^{127}I was of 2.18 x10^{-2} mM^{-1}.This represents an inter-day measurement variability of 20% compared to the RSF presented in Figure 13F. This is considered acceptable especially since the new calibration curve incorporate more data points. Additionally, the RSF for ^{81}Br was 7.52 x10^{-3} mM^{-1}. A similar LOD_{127I} and LOQ_{127I} was also obtained. The LOD_{127I} was estimated at ≈2 µM and LOQ_{127I} at ≈6 µM, based on $^{127}I^-/^{13}C^{12}C^-$ measurements of a blank Agar 100 resin. Similarly, LOD_{81Br} was estimated at ≈16 µM and

$LLOQ_{81Br}$ at ≈50 µM based on $^{81}Br^-/^{13}C^{12}C^-$. Therefore, to quantify ^{81}Br-labeled drugs, eq.4 was applied.

$$[^{81}Br.drug] = \left(\frac{^{81}Br^-}{^{13}C^{12}C^-}_{sample} - \frac{^{81}Br^-}{^{13}C^{12}C^-}_{control} \right) \times \frac{1}{N^{127}Br} \times \frac{1}{RSF_{81Br}} \quad (4)$$

Bromide has two stable isotopes, ^{79}Br and ^{81}Br, with a natural abundance of ≈51% and ≈49%, respectively. Here, I arbitrarily decided to focus on the ^{81}Br isotope, but it was determined that the ^{79}Br isotope has the same RSF as the ^{81}Br, and that to quantify both isotopes, their respective RSFs could be summed.

4.2.3. Quantification via ^{19}F

In some rare cases, ASOs incorporate 2'-fluoro modifications at the 2´-O position of the ribose (Figure 8) which increases binding affinity.[65] Moreover, the fluoro substitution is frequently applied to siRNAs.[65, 67, 68] Notably, three GalNAc-conjugated siRNAs already approved in the clinic present several 2´-fluoro modifications.[138] Therefore, I decided to add that option to the NanoSIMS quantification toolbox.

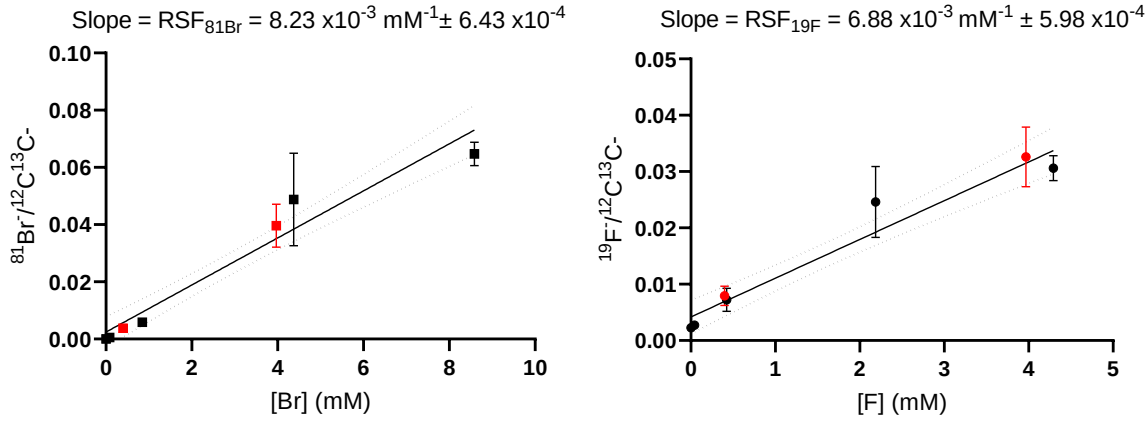

Figure 16. Bromide and fluoride calibration curves. EpoxyCure 2 resin was spiked with a known amount of either 2,6-dibromo-3-chloro-4-fluoroaniline (in black) or 1-bromo-4-fluorobenzene (in red). 95% confidence interval bands are represented by the dotted lines.

In line with previous standard preparation, different amounts of either 2,6-dibromo-3-chloro-4-fluoroaniline or 1-bromo-4-fluorobenzene were spiked in the resin, where the bromide component of the molecule serves as an internal standard. Since the 2,6-dibromo-3-chloro-4-fluoroaniline contains two bromide atoms, it is important to use the millimole equivalent per liter notation to be able to compare both molecules. Here, we used EpoxyCure2 resin for ease of use as the curing can be performed at ambient conditions and at room temperature.

An RSF of 8.23 x10^{-3} mM^{-1} was obtained for ^{81}Br (Figure 16). This represents an acceptable ≈10% inter-measurement variability compared to the previous RSF of 7.52 x10^{-3} mM^{-1}. The LOD for ^{81}Br was estimated at ≈4 µM and the LOQ for ^{81}Br at ≈14 µM, based on $^{81}Br^-/^{13}C^{12}C^-$ measurements (1.12 x10^{-5}) of a blank Epoxycure2 resin.

Therefore, it was estimated that the RSF for ^{19}F of 6.88 x10^{-3} mM^{-1} was reliable. The LOD for ^{19}F was estimated at 105 µM and the limit of quantification LOQ for ^{19}F at 317 µM based on the standard deviation of $^{19}F^-/^{13}C^{12}C^-$ ratio (2.49 x10^{-4}) of blank resin measurements. Similar to other halogens, the ^{19}F labeled drug concentration can be calculated with eq. 5.

$$[^{19}F.drug] = \left(\frac{^{19}F^-}{^{13}C^{12}C^-}_{sample} - \frac{^{19}F^-}{^{13}C^{12}C^-}_{control} \right) \times \frac{1}{N^{19}F} \times \frac{1}{RSF_{19F}} \quad (5)$$

4.3. Quantification of the less abundant and heteregenously distributed ^{34}S isotope (Paper I)

The PS backbone modification is broadly used in ASOs approved for commercial use or under development.[65] The replacement of a non-bridging oxygen atom with a sulfur atom can be advantageously exploited to incorporate a stable sulfur isotope (^{34}S) during the ASO synthesis.[139, 140] This can be done without changing the ASO sequence and the sulfur isotope can then be detected by NanoSIMS.[56, 140-142] Therefore, I also sought to develop an absolute quantification approach using ^{34}S.

Contrary to ^{127}I and ^{81}Br, biological samples have a highly variable sulfur content, especially in ^{32}S. Therefore, based on the isotopic natural abundance of the sulfur atom, 4.25% of the ^{32}S signal will influence the ^{34}S signal. Thus, ^{34}S enrichments could appear diluted in local dense ^{32}S regions, and vice versa. Therefore, it was necessary to express the ^{34}S enrichments in terms of excess in relation to the ^{32}S density (eq. 6) and the average $^{34}S^-/^{32}S^-$ ratio of a control cell ($\mu_{control} \approx 0.045$, which is very similar to the Carbon Diablo Troiloite (CDT) reference material were $^{34}S^-/^{32}S^- = 1/22.22$). Then, the excess was normalized by the $^{13}C^{12}C^-$ constant background and divided by the number of ^{34}S labels.

$$[^{34}S.drug] = \left(\frac{^{34}S^-_{sample} - (^{32}S^-_{sample} \times \mu_{control})}{^{13}C^{12}C^-} \right) \times \frac{1}{N^{34}S} \times \frac{1}{RSF_{34S}} \quad (6)$$

The ^{34}S external standards were prepared by spiking the Agar 100 resin with known amounts of a ^{34}S-labeled omeprazole (Figure 17). Here, ASOs couldn´t be used due to poor solubility in the resin. DMSO was also used to spike the Agar 100 resin. In that case, the ^{34}S content of the standards was calculated by dividing the DMSO concentration by the ^{34}S abundance of the CDT reference material (1/22.22 = 4.5 %). The calibration curve was drawn, and an RSF_{34S} of 5.37 x 10^{-3} mM^{-1} was found. The LOD for ^{34}S was ≈5 µM and the LOQ for ^{34}S was ≈14 µM based on the standard deviation of $^{34}S^-/^{13}C^{12}C^-$ ratios measured on a blank resin. The NanoSIMS data can then be transformed to determine concentration by multiplying the $^{34}S_{15}$-ASO excess by 1/RSF (eq. 6).

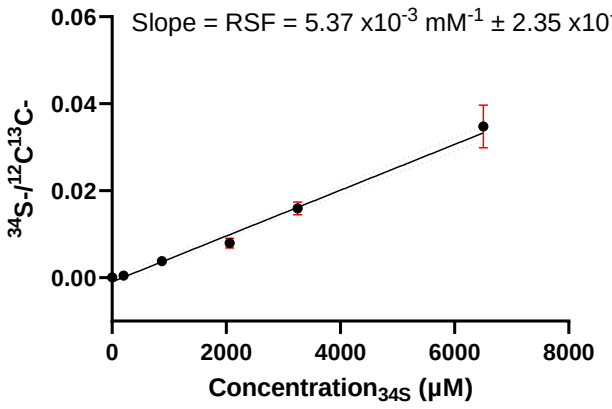

Figure 17. ^{34}S calibration curve. Agar 100 resin was spiked with known amount of either ^{34}S-omeprazole or DMSO. 95% confidence interval bands are represented by the dotted lines.

4.4. Validation of the quantification by comparing $^{127}I_2$-ASO, Br_4-ASO and $^{34}S_{15}$-ASO (Paper I & II)

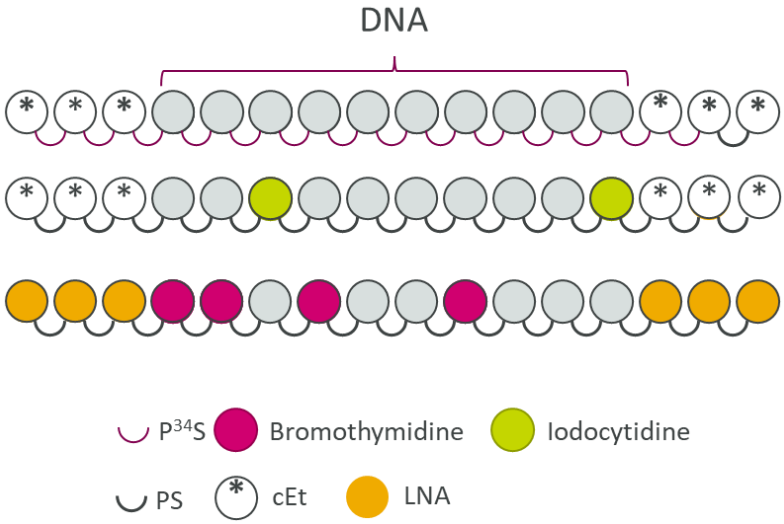

Figure 18. Schematic representation of the $^{127}I_2$-ASO, Br_4-ASO and $^{34}S_{15}$-ASO. Here, we used a tool gapmer ASO to target the ubiquitously expressed MALAT1 long non-coding mRNA for which the sequence is G-C-A-T-T-C-T-A-A-T-A-G-C-A-G-C.

To validate our quantification, we compared the intracellular concentration of an unconjugated ASO labeled with either elemental (iodide or bromide) or isotopic (^{34}S) labeling (Figure 18). As expected, the three ASO-enriched populations were not significantly different in terms of concentration, showing the robustness of our quantification methodology for the ^{127}I, ^{81}Br and ^{34}S labels (Figure 19).

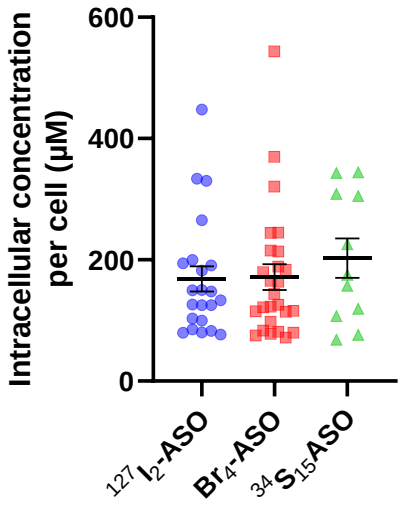

Figure 19. Quantification of a Malat1 ASO. Primary human hepatocyte spheroids were incubated with 5 µM of either $^{127}I_2$-ASO or $^{34}S_{15}$-ASO for 24 h or Br_4-ASO for 26 h. Mean ± standard error of the mean.

4.5. Conclusions

The systematic use of absolute quantitative NanoSIMS has been limited by the lack of adequate standards. Here, we introduced a simple methodology to prepare external standards for absolute quantification by NanoSIMS. This allowed us to provide quantification for several

halogen labels (^{127}I, ^{81}Br and ^{19}F) and for one isotopic label (^{34}S) that can be easily incorporated into the structure of ASOs (Table 1). Each of these strategies are an improvement compared to the ^{13}C approach in terms of sensitivity. By expanding the NanoSIMS quantification toolbox, it is possible to combine different labeling strategies to investigate the subcellular distribution and quantification of different ASOs in the same cells (paper II and V), as well as different moieties of the compound (Paper IV).

Table 1 summarizes the RSFs, LODs, and LOQs that were determined and later used in the different publications included in this thesis. Note that a difference is observed in LOD and LOQ between the blank resin and the cell for the ^{34}S and the ^{19}F due to the non-homogeneous and/or high background, respectively. So similarly, the LOD was calculated as (3.3 x $\sigma_{control}$)/RSF and LOQ = (10 x $\sigma_{control}$)/RSF, where $\sigma_{control}$ represents the standard deviation of the different ratios of interest in hepatocytes. Similar to ^{13}C, incorporating several labels will allow improvement in the LOD and LOQ. A rough estimation will be to divide the LODs and LOQs reported in Table 1 by the number of labels incorporated in the molecule of interest.

Table 1. Summary of the RSFs obtained for the different labeling strategies, and the associated LOD and LOQ.

	RSF ± Stdd error (mM^{-1})	LOD_{blank}*	LOQ_{blank}*	$\sigma_{controlcell}$	LOD_{cell}*	LOQ_{cell}*
^{127}I	$2.18 \times 10^{-2} \pm 9.43 \times 10^{-4}$	2	6	4.10×10^{-5}	6	19
^{81}Br	$7.52 \times 10^{-3} \pm 1.56 \times 10^{-4}$	16	50	4.44×10^{-5}	19	59
^{34}S	$5.37 \times 10^{-3} \pm 2.35 \times 10^{-4}$	5	14	7.34×10^{-4}**	451	1366
^{19}F	$6.88 \times 10^{-3} \pm 5.98 \times 10^{-4}$	105	317	1.45×10^{-3}	631	2104

*LOD and LOQ are expressed in µM for 1 label. ** The local variation in sulfur in ROIs will affect its LOD and LOQ, so here the $\sigma_{control}$ for ^{34}S was measured on resin spiked with 140 mM DMSO to obtain a homogeneous sullfur background and mimic the average sulfur content of hepatocytes.

Chapter V. Study of ASOs uptake and trafficking by NanoSIMS.

5.1. Investigating the uptake and trafficking of PS-ASOs and GalNAc-ASOs

Many questions remain unresolved concerning the uptake, subcellular distribution and endosomal escape of ASOs. Furthermore, there is no real information on the concentration of ASOs at the intracellular site of action required to trigger their pharmacological effect. Here, I sought to increase our understanding using the quantitative NanoSIMS approach. [58, 142]

In this chapter, several labeled PS-ASOs and GalNAc-PS-ASOs are used (Figure 20). These ASOs contain a PS backbone modification that leads to facilitated ASO internalization by interacting with cell surface proteins which in turn impacts the cellular uptake of ASOs, their intracellular trafficking, and potency.[62, 96, 97, 143]

Here, the different gapmers specifically target the long non-coding RNA metastasis-associated lung adenocarcinoma transcript 1 (*MALAT1*) which is abundantly expressed and well conserved in various species. *MALAT1* is involved in several physiological functions and has also been identified as a prognostic marker in various diseases like cancer, cardiovascular and neurodegenerative diseases.[144-150] Hence, ASO-mediated knockdown of *MALAT1* could play a potential role as a therapeutic strategy. Nonetheless, here *MALAT1* represents a simplified and straightforward readout of ASO potency as it is not a protein-coding transcript.[151, 152] Indeed, ASOs that target protein-coding genes require downstream analysis to determine the effect of ASO-mediated knockdown on protein expression. It is also important to note that, when looking at the subcellular distribution of ASOs, *MALAT1* has an overall nuclear positioning and is also present in the cytoplasm in lower amounts.[149, 153-155]

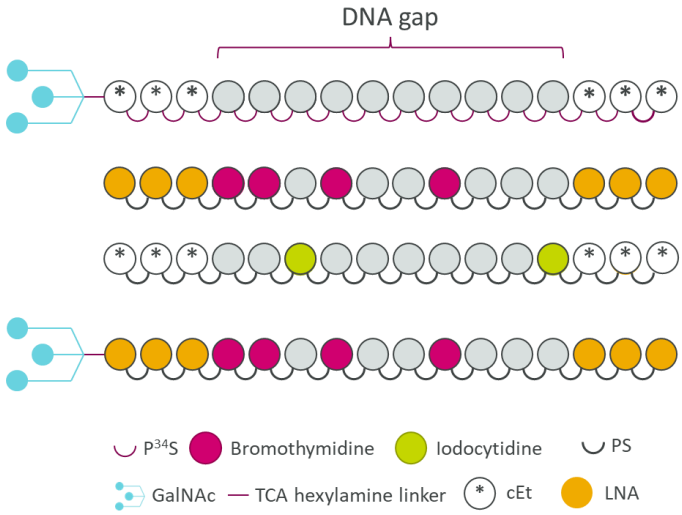

Figure 20. Schematic representation the different PS-ASOs and GalNAc-PS-ASO compounds.

5.1.1. Saturation of ASO uptake (Paper I & II)

It is commonly accepted that conjugated and unconjugated PS-ASOs enter cells via endocytosis. However, endocytosis is a general term that refers to a variety of internalization pathways. Unconjugated ASOs are delivered to cells via a process called gymnosis (a type of endocytosis by which ASOs are delivered to cells in the absence of any carriers or conjugation), whereas conjugation to a ligand such as GalNAc leads to receptor-mediated endocytosis. Previously, it was demonstrated that the PS composition of ASOs can also affect ASGPR

binding.[96, 156] Specifically, high concentrations of full PS backbone ASOs compete with the GalNAc moiety to bind to the ASGPR.[112, 157] It has also been shown that GalNAc- PS-ASO [118] and PS-ASO [156] uptake are saturated in a dose-dependent manner.

To demonstrate the utility of the quantitative NanoSIMS method I sought to investigate the distinct characteristics of the endocytic pathway utilized by either an unconjugated PS-ASO (Br_4-labeled) or a GalNAc-PS-ASO conjugate ($^{34}S_{15}$-labeled). Indeed, the endocytic pathway matters and can be exploited to benefit ASOs uptake and trafficking.

First, I noted that both the PS-ASO and GalNAc-PS-ASO accumulate in electron dense structures after 24 h incubation (presumably lysosomes), by correlating NanoSIMS imaging and electron microscopy, which is in accordance with the literature.[65, 81, 158]

With increasing unconjugated PS-ASO dose, the intracellular concentration increases and then reaches an uptake plateau around the 1 µM dose as shown in Figure 21, but the increase is not proportional to the dose. Data show that GalNAc-PS-ASO uptake does not saturate in this concentration range and demonstrates increased uptake albeit non-linear at higher concentrations compared to PS-ASO. This might be explained by the fact that GalNAc ligands interact specifically with the high turnover ASGPR, while the unconjugated PS-ASO interacts non-specifically with a multitude of cell surface proteins with finite capacity.[104, 112, 118, 158, 159]

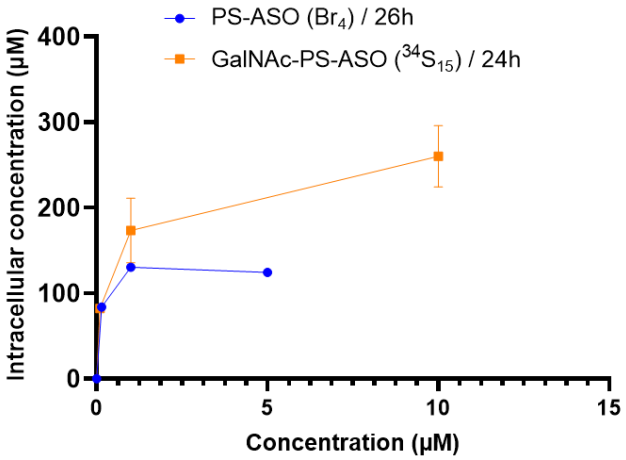

Figure 21. Comparison of the dose-dependent uptake of a PS-ASO (bromide labeled) and its GalNAc-PS-ASO version ($^{34}S_{15}$ labeled) in PHH spheroids following 26 h or 24 h incubations, respectively. The ASGPR mediated endocytosis allows more uptake of ASO than gymnosis. Plus, the uptake of PS-ASO reaches a plateau at lower concentrations while the uptake of GalNAc-PS-ASO continues to increase. Mean ± standard errors of the mean are reported.

This also indicates that the incubation concentrations do not directly relate to the concentrations inside the cell. Hence, the intracellular concentration measurement is fundamental to all events which occur downstream, including endosomal escape and gene silencing. The data also indicated that iodide or bromide should be the preferred labels to explore low enrichments or to investigate ASO intracellular concentration at early time points.

5.1.2. Trafficking of ASOs (Paper III)

ASO internalization and trafficking is a well-orchestrated process and endolysosomal vesicles move through the cytosol via a polarized network of microtubules.[160] It was shown that colchicine disrupts the microtubule network and alters ASO trafficking, leading to a reduced release of ASO from late endosomes and impairing knockdown activity.[123] Therefore, it was decided to use NanoSIMS to quantify the effect of colchicine on the uptake, accumulation and distribution of both a GalNAc-PS-ASO (Br-labeled) and an unconjugated ASO (I-labeled).

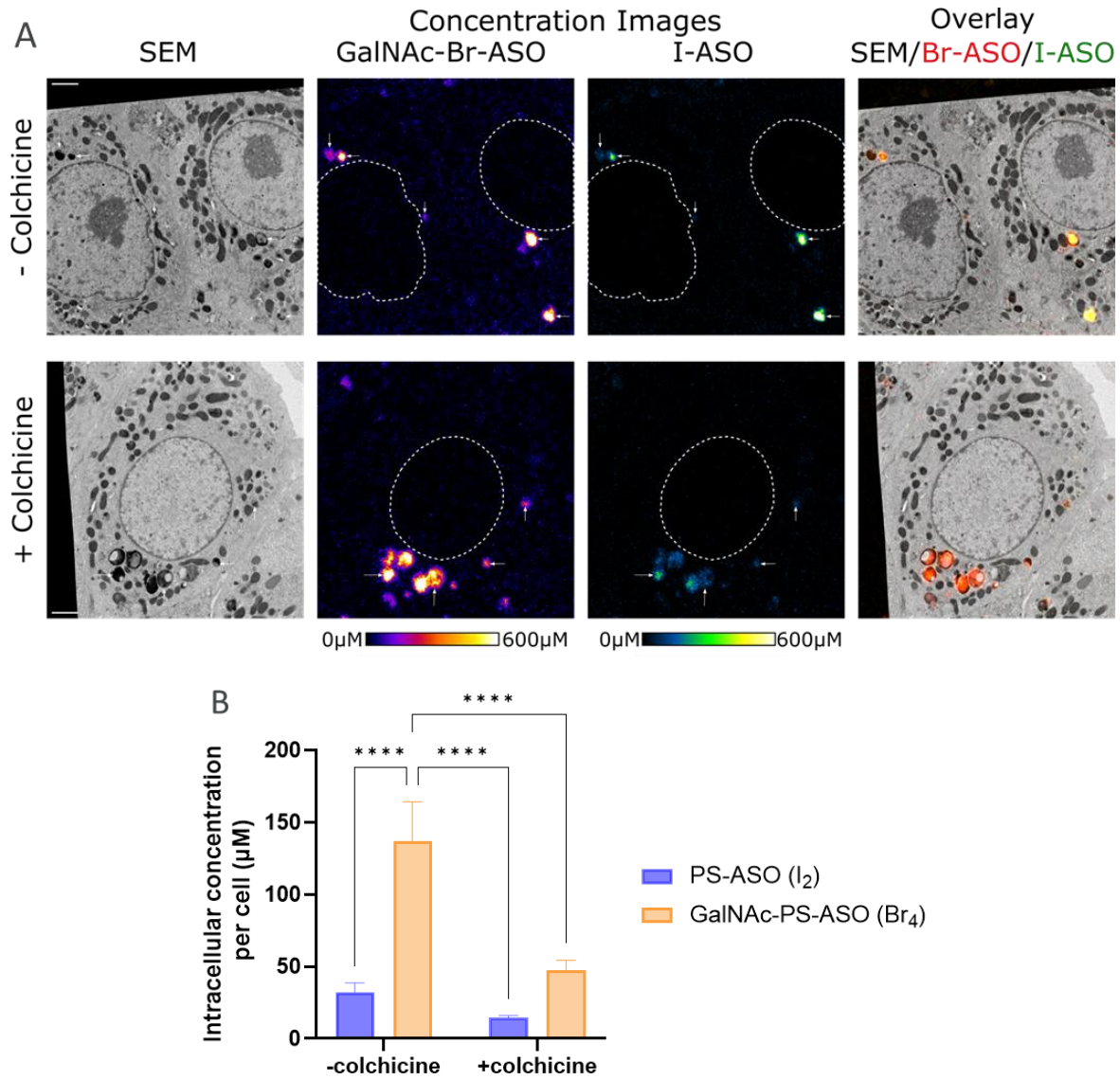

Figure 22. Colchicine affects ASO uptake. PHH were co-incubated with 1 µM GalNAc-Br-ASO and 1 µM I-ASO for 6 h then supplemented with 0.15% final DMSO (- colchicine, n=5 images) or 0.15 µg/mL colchine (+ colchicine, n=5 images) for a total of 24 h and processed for electron microscopy and NanoSIMS analysis (A). The cell morphology is visualized by the SEM. Scale bars: 2 µm. Nuclei are highlighted on concentration images. The control cells (n=2 images) allowed to determine the average $^{81}Br^{-}$ /$^{13}C^{12}C^{-}$ = 4.71 x10^{-4} and $^{127}I^{-}$ /$^{13}C^{12}C^{-}$ = 2.10 x10^{-4} to calculate the ASOs concentrations via eq. 3 and 4 (B). Differences were assessed by two-way ANOVA, *** p-value = 0.0003. **** p-value <0.0001. Mean ± standard errors of the mean are reported.

As expected, the intracellular concentration of both GalNAc-PS-ASO and unconjugated PS-ASO differs (Figure 22) with ≈4 times more GalNAc-PS-ASO than unconjugated PS-ASO.

Upon colchicine treatment, the total intracellular concentration of GalNAc-Br-ASO is significantly reduced by a factor ≈3. The decrease is also observed to a lesser extent for the I-ASO. That indicates that co-administration of colchicine slows-down and could stop ASO uptake. As colchicine inhibits the microtubule network, it was hypothesized that the membrane proteins intervening in the uptake of the different PS-ASOs are trapped and not recycled back to the plasma membrane leading to too low amount at the cell membrane to induce further ASO uptake. In colchicine-treated cells ASOs accumulate in larger endolysosomal compartments that are positioned further away from the nucleus compared to non-treated cells. Thus, the reduction in knockdown activity observed by Liang *et al*. (2021) can be attributed to the reduction of the amount of ASO internalized and not only to the impairment of the positionning of LEs at the nucleus periphery.

5.1.3. Kinetics of ASOs uptake (Paper II)

Although internalization of ASO occurs rapidly, within 30 min, the target knockdown occurs later.[62, 110, 118, 125, 141, 158, 161] Therefore, to further explore the kinetics of ASO internalization, a NanoSIMS analysis of the intracellular concentrations and the subcellular distribution of both a GalNAc-PS-ASO (Br_4-labeled) and an unconjugated PS-ASO (I_2-labeled), was carried out simultaneously.

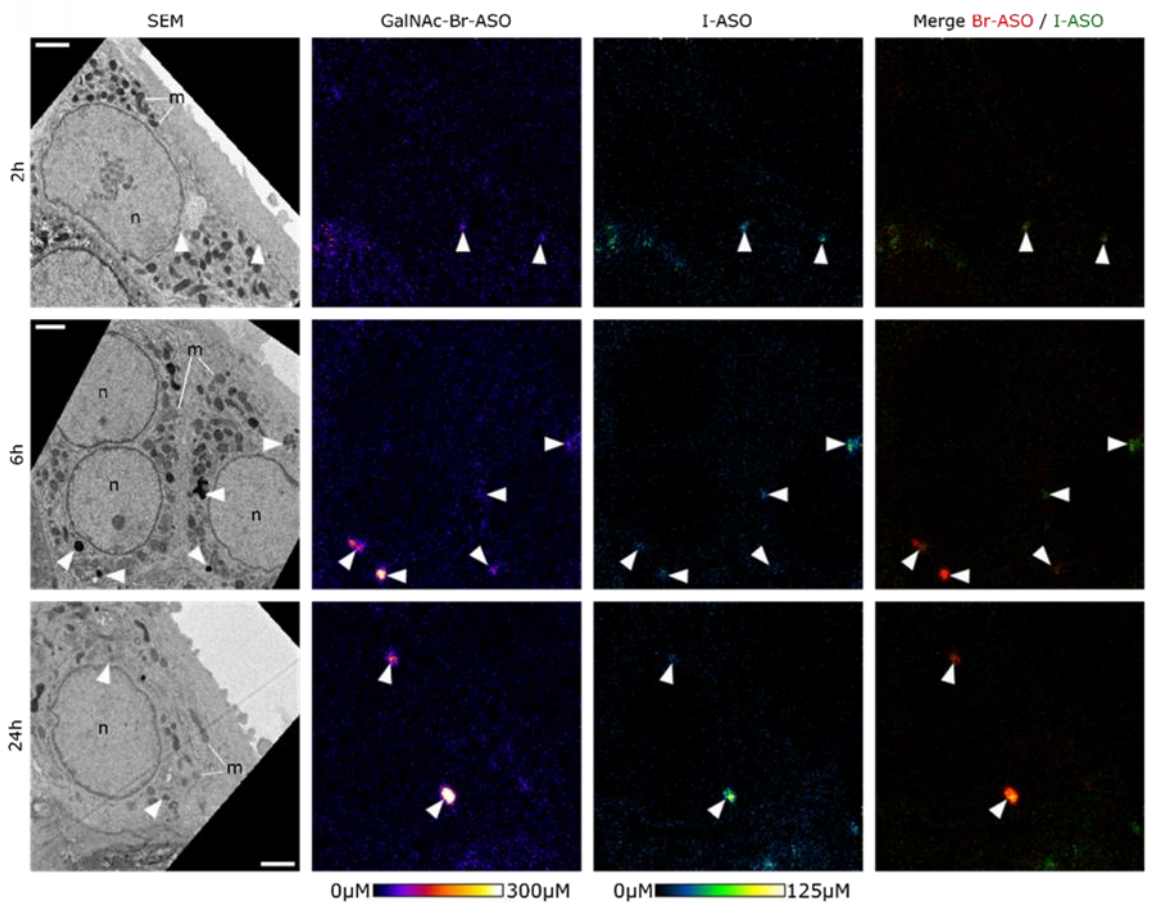

Figure 23. NanoSIMS imaging of the differential uptake between a GalNAc-Br-ASO and an unconjugated I-ASO by NanoSIMS. PHH spheroids were either untreated (n=4, 866 ROIs, µcontrol is 1.98 x 10^{-4} and 6.74x10^{-5} for $^{81}Br^-/^{13}C^{12}C^-$ and $^{127}I^-/^{13}C^{12}C^-$, respectively) or co-incubated with 100 nM I-ASO and 100nM GalNAc-Br-ASO for 2 h (n=5, 23 ROIs), 6 h (n=3, 29 ROIs) and 24 h (n=3, 47 ROIs) before being processed for SEM and NanoSIMS. Scale bar: 2µm. Arrows point out different cytosolic ASOs enrichments. n: nucleus, m: mitochondria.

Figure 23 shows ASOs subcellular distribution. Although I did not observe much overlap between the GalNAc-PS-ASO and PS-ASO signals at 2 h, longer incubations lead to more and more overlap between both ASOs. The longer incubations also lead to more accumulation of ASO as depicted by their respective intracellular concentrations (Figure 24) with ≈10 times more GalNAc-PS-ASO than unconjugated PS-ASO after 24 h incubation. These data are in accordance with the concept presented in several publications, that unconjugated and conjugated ASOs enter the cell via different mechanisms, where gymnosis (PS-ASO) is leading to lower internalization compared to ASGPR mediated uptake (GalNAc-PS-ASO) but share the same subcellular fate, i.e., accumulation in lysosomes.

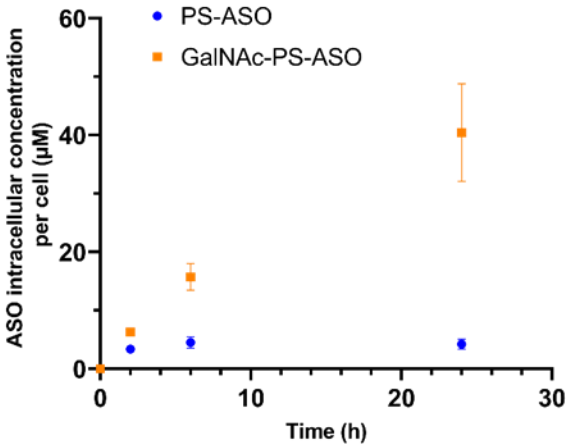

Figure 24. Quantification of the differential uptake between a GalNAc-Br-ASO and an unconjugated I-ASO by NanoSIMS. Uptake was quantified by applying eq. 3 and 4 to the $^{81}Br^-/^{13}C^{12}C^-$ and $^{127}I^-/^{13}C^{12}C^-$ ratios and after 24 h incubation a 10-fold difference in ASOs uptake could be visualized. Mean ± standard errors of the mean are reported.

5.2. Correlating intracellular concentration, number of molecules and RNA reduction (Paper II & III)

ASO molecules must be distributed to their site of action (≈60 min), then hybridized to their target (≈20 min), and recruit the RNase H (≈40 min) to degrade the RNA target. [62, 89, 162] In theory, it is possible to detect RNA reduction 2 h post incubation. However, the knockdown of the *MALAT1* RNA was measured after a 24 h incubation to maximize the percentage of reduction. This suggests that the number of ASO molecules inside a cell should relate to the reduction of the target level.

Since the depth of the NanoSIMS measurement is known, it is possible to calculate the volume of sample analyzed (here ≈10 fL/image). Thus, the intracellular concentrations can be translated to the number of ASO molecules using the volume of sample analyzed and Avogadro's constant (Figure 25). It is thus possible to estimate the number of molecules per cell using the reported volume of a human hepatocyte (~3000 μm^3)[163, 164] for 100 nM (Figure 24) and 1 µM (Figure 22) concentration of ASO after 24 h co-incubation and these values are summarized in Table 2.

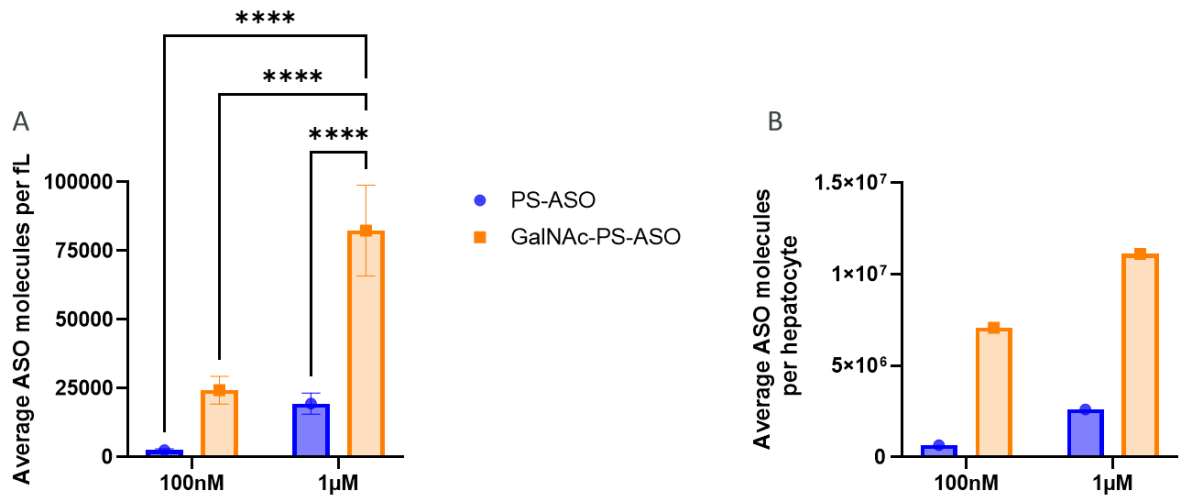

Figure 25. Number of molecules calculated based on data from figures 22 and 24, for the PHH spheroids co-incubated for 24 h with 100 nM or 1 µM of PS-ASO (I-labeled) and GalNAc-ASO (Br-labeled) (A). Differences were assessed by two-way ANOVA, **** p-value <0.0001. The number of ASO per femtoliter (fL) can be scaled to the volume of a hepatocyte (B) and can later be used to estimate the number of molecules that undergo 1% endosomal escape. Mean ± standard errors of the mean are reported.

Table 2. Summary of the intracellular concentrations, calculated number of ASO molecules per hepatocyte and the expected number of molecules undergoing 1% of endosomal escape.

$[ASO]_{incubation}$	Average $[ASO]_{intracellular}$ (µM)		ASO molecules/hepatocyte		ASO molecules/1% escape	
	PS-ASO	GalNAc-PS-ASO	PS-ASO	GalNAc-PS-ASO	PS-ASO	GalNAc-PS-ASO
100 nM	4.2	40.4	6.60×10^5	7.07×10^6	6.60×10^3	7.07×10^4
1 µM	32.3	136.8	2.60×10^6	1.11×10^7	2.60×10^4	1.11×10^5

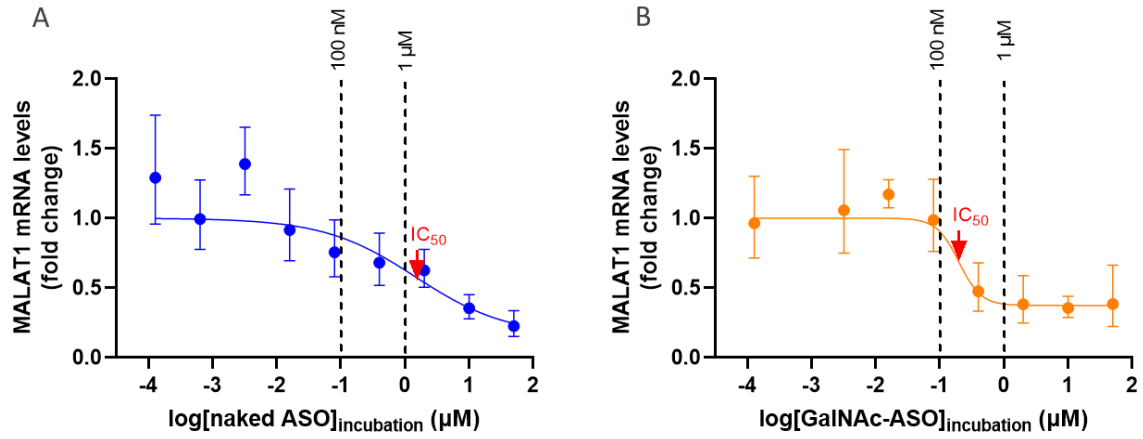

Figure 26. Dose-dependent reduction of levels of *MALAT1* mRNA following exposure to different ASOs. The effect of an unconjugated PS-ASO (A) and a GalNAc-PS-ASO (B) on MALAT1 transcript levels was assessed by RT-qPCR. Transcript levels were measured after treating spheroids with different ASO concentrations at 24 h. ASOs used here are not labelled. Dotted lines relate to the incubation concentration used for NanoSIMS experiments (100 nM or 1 µM). Mean ± margin of error (upper and lower limits for each points measured by qPCR) are reported.

In parallel, the effect of different concentrations of GalNAc-PS-ASO and unconjugated PS-ASO on *MALAT1* mRNA levels was measured by RT-qPCR (Figure 26). After 24 h incubation, 50% inhibition concentrations (IC_{50}) of ≈200nM and ≈1.5 µM are observed for the GalNAc-PS-ASO and PS-ASO, respectively. This confirms that at equal incubation concentrations, the GalNAc-PS-ASO is more potent. This is attributable to the higher uptake of the GalNAc conjugate. By combining *MALAT1* expression levels with the intracellular concentrations and related number of ASO molecules (Figure 25 and Table 2), I determined that between ≈70 000 and ≈111 000 molecules need to escape to reduce *MALAT1* by 50% (IC_{50} of 200 nM, Figure 26B) after 24 h incubation with a GalNAc-PS-ASO. For the PS-ASO the number of ASO molecules that need to escape to reach the IC_{50} (Figure 26A) will be above 26 000 molecules but will be related to a higher dose (PS-ASO incubation above 1 µM) and still lead to a less potent activity (IC_{50} of 1.5 µM). Hence, the conjugation to a GalNAc domain improves endosomal escape by loading more ASOs into hepatocytes compared to the PS-ASO at the same incubation concentration.

5.3. Investigating eGLP1 ASO and the impact of the linker chemistry (Paper IV)

The extrahepatic delivery of ASOs remains a challenge. ASOs conjugated to eGLP1 peptide have recently demonstrated a potential for targeting pancreatic beta cells via the GLP1R.[108, 109, 165] Thus, it was decided to investigate the uptake and trafficking of an eGLP1 conjugated via a maleimide linker to a MALAT1-ASO. In this study, the eGLP1 conjugate was labeled with two iodide atoms whereas the ASO was labeled with 15 x ^{34}S isotopes. Therefore, following both the targeting ligand and the ASO provided a more complete picture of the subcellular distribution and accumulation of ASOs which can be crucial to optimize their therapeutic efficacy.

Based on fluorescent microscopy data, 30 min incubations were used for the eGLP1 conjugate to probe endosomes instead of lysosomes.[81] NanoSIMS data indicated that eGLP1 hotspots were found in empty looking structures on the $^{12}C^{14}N$ images (Figure 27A), presumably endosomes as verified by electron microscopy. However, $^{34}S_{15}$-ASO enrichments could not be visualized in the same structure.

It was speculated that the ligand and ASO were decoupled. Indeed, during the endosome maturation, a progressive acidification of the endosomal compartment occurs. First, this leads to the separation of the PS-ASO and the endocytic receptor.[81, 110, 166-168] Then, this acidification can also impact the stability of the PS-ASO conjugate. Therefore, a new conjugate was designed by incorporating a more stable linker (Figure 28), switching from a maleimide linker to a bicyclononyne linker (BCN).[169, 170] The new compound also incorporated more ^{34}S isotopes ($^{127}I_2$-eGLP1$_{BCN}$-$^{34}S_{19}$-ASO) to enhance ASO detection by NanoSIMS.

The intracellular concentrations of both the $^{27}I_2$-eGLP1-$^{34}S_{15}$-ASO and the $^{127}I_2$-eGLP1$_{BCN}$-$^{34}S_{19}$-ASO were quantified (Figure 29). It was hypothesized that if the PS-ASO was still attached to the eGLP1 moiety, then their respective intracellular concentrations should provide a 1:1 ratio with the more stable linker. Here, the data were reanalyzed by multiplying the published data by the appropriate RSF since at the time of the publication they were not readily available. Increasing the stability of the linker ($^{127}I_2$-eGLP1$_{BCN}$-$^{34}S_{19}$-ASO) and/or the number of ^{34}S isotopes in the compound allowed the detection of $^{34}S_{19}$-ASO enrichments overlapping with the eGLP1 ligand (Figure 27B). The $^{127}I_2$-eGLP1$_{BCN}$-$^{34}S_{19}$-ASO leads to an increase of

detected enrichments aligning with 1:1 ratio line, suggesting that increasing the stability of the linker leads to increase fraction of intact eGLP1 conjugate. This data set also indicates that iodide or bromide should be the preferred labels to explore low ASO enrichments or investigations at early time points to facilitate enrichment visualization and data analysis.

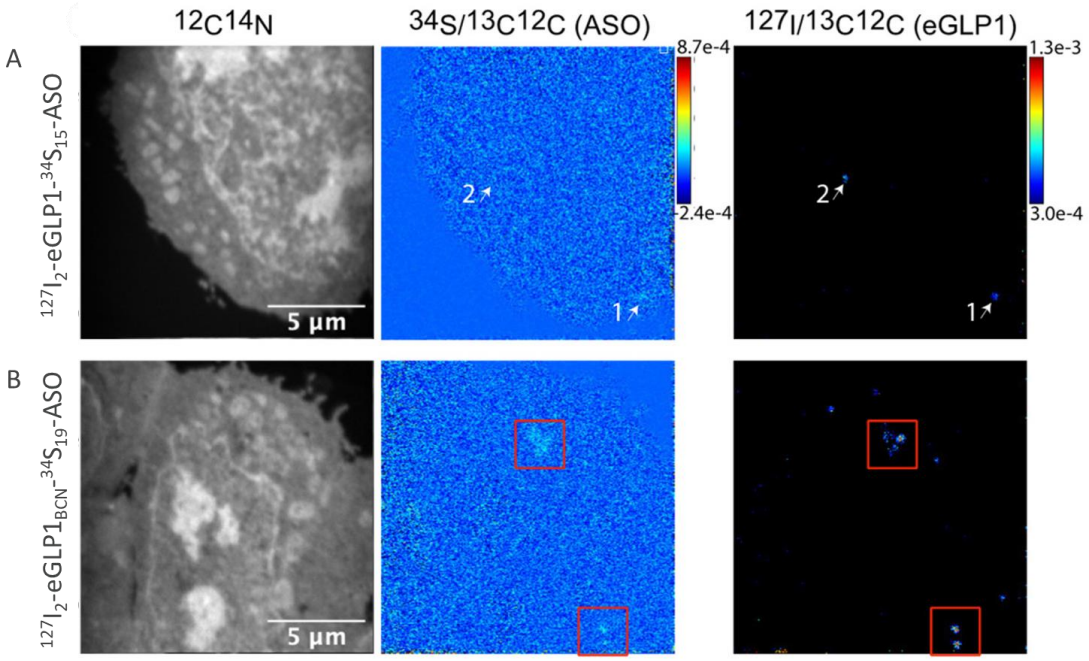

Figure 27. NanoSIMS imaging of an HEK293 cell overexpressing GLP1R treated with 1 µM of either $^{127}I_2$-eGLP1-$^{34}S_{15}$-ASO (A) or $^{127}I_2$-eGLP1$_{BCN}$-$^{34}S_{19}$-ASO (B) for 30 min. The $^{12}C^{14}N$ image shows the cell morphology $^{34}S/^{13}C^{12}C$ (ASO) and ^{127}I-/$^{13}C^{12}C$ (eGLP1) images are scaled to the carbon and their respective number of labels. This corresponds to eq. 3 and 6 before applying the RSF. For the treatment with $^{127}I_2$-eGLP1-$^{34}S_{15}$-ASO, eGLP1 hotspots can be seen but no ASOs hotspots seem to be associated to them. Increasing the stability of the linker ($^{127}I_2$-eGLP1$_{BCN}$-$^{34}S_{19}$-ASO) and/or the number of ^{34}S isotopes in the compound allows visualization of $^{34}S_{19}$-ASO enrichments overlapping with the eGLP1 hotspots.

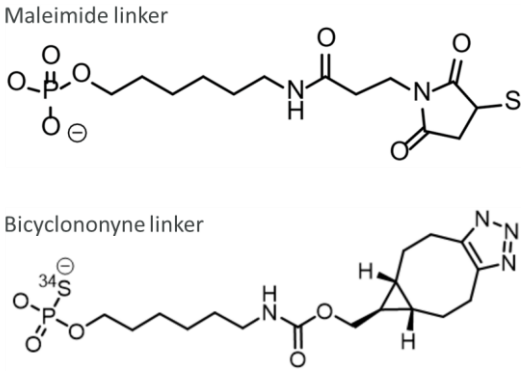

Figure 28. The different linkers used for the eGLP1-ASO. The bicyclononyne (BCN) linker, which is more stable than the maleimide linker, is used to investigate the potential cleavage of the eGLP1 moiety from the PS-ASO.

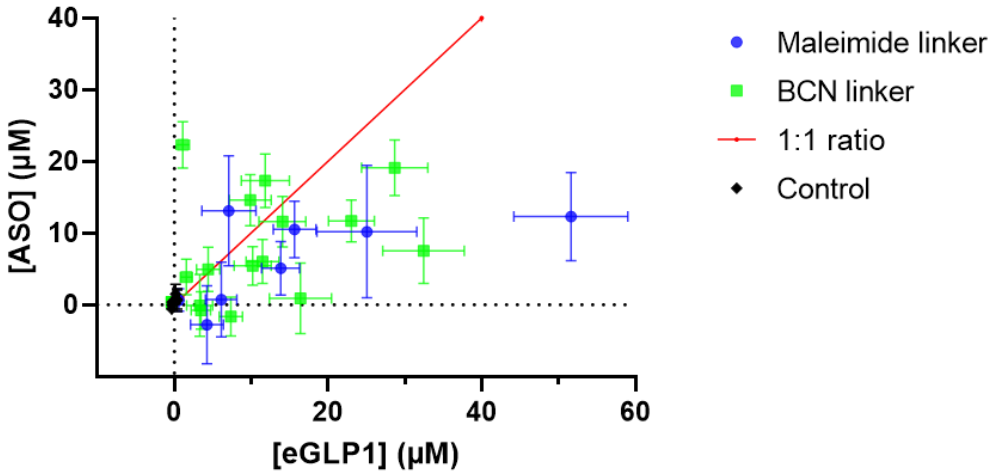

Figure 29. Quantification of a $^{127}I_2$-eGLP1-$^{34}S_{15}$-ASO with a maleimide linker and $^{127}I_2$-eGLP1$_{BCN}$-$^{34}S_{19}$-ASO with a BCN linker after 30 min incubation. Intact eGLP1-ASO signal should align on the 1:1 ratio line.

5.4. Conclusions

Understanding the subcellular distribution and intracellular concentrations of ASOs is possible with NanoSIMS imaging. After 24h incubation, both unconjugated PS-ASOs and GalNAc-PS-ASOs accumulate in lysosomes in hepatocytes which is consistent with the literature. It was also shown that ASO uptake is saturable both in a concentration and time-dependent manner. This work also demonstrated that NanoSIMS is a reliable tool to investigate the impact of small molecules on ASO trafficking in cells. Importantly, the data show that NanoSIMS quantification can be used to correlate intracellular concentration and ASO potency. Thanks to our different labeling strategies, it was proven that fine chemistry tuning can have a great influence on ASO subcellular distribution. Therefore, following both the targeting domain and the ASO could provide better understanding of endosomal escape mechanisms.

OUTLOOKS

NanoSIMS imaging offers unique insights into the cellular distribution of ASOs by assessing their uptake and subcellular accumulation and connecting this to their biological function. This work also provides an analysis template to investigate the effectiveness of newly developed targeting domains. This represents an opportunity to hasten and strengthen the development of new oligonucleotide therapeutics. Particularly considering that the relationship between intracellular concentration and biological activity of ASOs can be a key factor in treating pathologies beyond liver diseases.[66, 67, 108, 171, 172]

Now, one may also be able to describe endolysosomal escape rate more thoroughly using the NanoSIMS quantification approach presented here. Indeed, precisely pinpointing the localization and timing of ASO escape would offer mechanistic insights into their efficacy as therapeutics.[82, 83, 111, 173] Different types of small-molecule drugs can be used to manipulate the endolysosomal system to better appreciate the underlying mechanisms behind ONTs endosomal escape and trafficking.[82, 83, 113, 114] Hence, another interesting approach would be to investigate the subcellular distribution and quantification of both the ONT and the endosomal escape agent. For example, one could use the ONT/endosomal escape agent ratio to determine the appropriate ratio that leads to endosomal escape and detection of ONT at site of action, which in return would be useful for therapeutic dose determination.

This approach can also be used to investigate other drugs as halogenated drugs are increasingly emerging in the pipeline of pharmaceutical companies.[174] For example, siRNAs frequently contain fluoride atoms in their structures.[138, 175, 176] The drawback here would be that the fluoride quantification is not the most sensitive approach due to a relatively noisy background (Table 1), that we think is related to the sample preparation. Additionally, the fluoride atoms tend to be incorporated into both strands of the siRNAs. Thus, it is not possible to distinguish the sense strand from the antisense strand which is carrying the gene silencing property. Adding a halogen label (iodide or bromide), at least in the antisense strand, could be an option. This will make it possible to determine the intracellular fate of both strands and obtain a sense/antisense strands ratio to further characterize the biodistribution of siRNAs at the subcellular level. This holds true for small activating RNAs as well, which have the same double-stranded structure as siRNAs but work to enhance gene expression rather than decrease it.[177]

Despite these numerous possibilities, it is essential to consider the fixability of the target molecule and the concentration required for NanoSIMS detection, in relation to the LODs reported in this thesis (Table 1), before beginning such quantification experiments. Another factor to consider is the sensitivity, which is correlated with the number of labels that can be placed into the chemical structure of the target molecule. Indeed, the sensitivity will increase with the number of labels (Figure 27), but that could impair the chemical and biological properties of the target molecule. Moreover, despite being a highly sensitive method, NanoSIMS does not offer the highest throughput. Thus, only a few therapeutic compounds of interest can be evaluated using this method in a comparative manner and NanoSIMS should be used at crucial stages of the drug development cascade to balance the throughput issue.

ACKNOWLEDGMENTS

To my supervisors, Andrew Ewing and Michael Kurczy, thank you for giving me the opportunity to do a PhD in this great environment. Your support and guidance have been invaluable in shaping my project. I am also thankful for the freedom you gave me to conduct my research. I have gained so much! I would also like to thank Shalini Andersson, Rasmus Jansson Löfmark and Constanze Hilgendorf for making my research at AstraZeneca possible, as well as John Fletcher for being my examiner.

Mike, thank you for spending so much time with me at the NanoSIMS. Your enthusiasm and our conversations made the basement more lively and fun. One day "NanoSIMS will cure all diseases"! I am also in great debt to Aurélien for teaching me the ways of the NanoSIMS in French, which made it easier. Elias, thank you for the countless hours you spent taking care of the instrument.

A big thank you to the ADME team at AstraZeneca for your kindness and support on a daily basis, as well as the whole team at the Ewing group for welcoming me.

To all the co-authors of the papers in my thesis, thank you for all the great discussion. Quentin and Rouven, thank you for providing the ASOs. I know the purification was not always easy...

To my friends, thank you for all the funny moments and all the interesting stories. This time will not have been the same without you.

To my family, thank you for always believing in me and supporting me in whatever I do. Mais maintenant j´arrête! Il n´y a pas de diplôme au dessus du PhD. Et merci pour les colis remplis de trucs français, c´est ridicule mais un petit biscuit par ci par là ça fait du bien au moral.

To Tom, thanks for the microteaching in oligonucleotide chemistry. More importantly, thank you for your support during these years. Having you around made the troubles go away. Thanks for the time we spent together; that was always a good time, even when camping and mud were involved.

REFERENCES

1. Dollery, C. T., Intracellular drug concentrations. *Clin Pharmacol Ther* **2013,** *93* (3), 263-6.
2. Hann, M. M.; Simpson, G. L., Intracellular drug concentration and disposition--the missing link? *Methods (San Diego, Calif.)* **2014,** *68* (2), 283-5.
3. Smith, D. A.; Di, L.; Kerns, E. H., The effect of plasma protein binding on in vivo efficacy: misconceptions in drug discovery. *Nature reviews. Drug discovery* **2010,** *9* (12), 929-39.
4. Rizk, M. L.; Zou, L.; Savic, R. M.; Dooley, K. E., Importance of Drug Pharmacokinetics at the Site of Action. *Clin Transl Sci* **2017,** *10* (3), 133-142.
5. Lin, J.; Sahakian, D. C.; de Morais, S. M.; Xu, J. J.; Polzer, R. J.; Winter, S. M., The role of absorption, distribution, metabolism, excretion and toxicity in drug discovery. *Curr Top Med Chem* **2003,** *3* (10), 1125-54.
6. Cobice, D. F.; Goodwin, R. J.; Andren, P. E.; Nilsson, A.; Mackay, C. L.; Andrew, R., Future technology insight: mass spectrometry imaging as a tool in drug research and development. *Br J Pharmacol* **2015,** *172* (13), 3266-83.
7. Solon, E. G., Autoradiography techniques and quantification of drug distribution. *Cell Tissue Res* **2015,** *360* (1), 87-107.
8. Spracklin, D. K.; Chen, D.; Bergman, A. J.; Callegari, E.; Obach, R. S., Mini-Review: Comprehensive Drug Disposition Knowledge Generated in the Modern Human Radiolabeled ADME Study. *CPT Pharmacometrics Syst Pharmacol* **2020,** *9* (8), 428-434.
9. Penner, N.; Xu, L.; Prakash, C., Radiolabeled absorption, distribution, metabolism, and excretion studies in drug development: why, when, and how? *Chem Res Toxicol* **2012,** *25* (3), 513-31.
10. Arranz, A.; Ripoll, J., Advances in optical imaging for pharmacological studies. *Front Pharmacol* **2015,** *6*, 189.
11. Hughes, L. D.; Rawle, R. J.; Boxer, S. G., Choose your label wisely: water-soluble fluorophores often interact with lipid bilayers. *PLoS One* **2014,** *9* (2), e87649.
12. Grimm, J. B.; Lavis, L. D., Caveat fluorophore: an insiders' guide to small-molecule fluorescent labels. *Nat Methods* **2022,** *19* (2), 149-158.
13. Vermeulen, I.; Isin, E. M.; Barton, P.; Cillero-Pastor, B.; Heeren, R. M. A., Multimodal molecular imaging in drug discovery and development. *Drug discovery today* **2022,** *27* (8), 2086-2099.
14. Licha, K.; Olbrich, C., Optical imaging in drug discovery and diagnostic applications. *Adv Drug Deliv Rev* **2005,** *57* (8), 1087-108.
15. Pien, H. H.; Fischman, A. J.; Thrall, J. H.; Sorensen, A. G., Using imaging biomarkers to accelerate drug development and clinical trials. *Drug discovery today* **2005,** *10* (4), 259-66.
16. Xue, Y.-J.; Gao, H.; Ji, Q. C.; Lam, Z.; Fang, X.; Lin, Z.; Hoffman, M.; Schulz-Jander, D.; Weng, N., Bioanalysis of drug in tissue: current status and challenges. **2012,** *4* (21), 2637-2653.
17. Beaumont, C.; Young, G. C.; Cavalier, T.; Young, M. A., Human absorption, distribution, metabolism and excretion properties of drug molecules: a plethora of approaches. *Br J Clin Pharmacol* **2014,** *78* (6), 1185-200.
18. Nilsson, A.; Goodwin, R. J.; Shariatgorji, M.; Vallianatou, T.; Webborn, P. J.; Andrén, P. E., Mass spectrometry imaging in drug development. *Analytical chemistry* **2015,** *87* (3), 1437-55.
19. Nwabufo, C. K.; Aigbogun, O. P., Potential application of mass spectrometry imaging in pharmacokinetic studies. *Xenobiotica* **2022,** *52* (8), 811-827.
20. Goodwin, R. J. A.; Takats, Z.; Bunch, J., A Critical and Concise Review of Mass Spectrometry Applied to Imaging in Drug Discovery. *SLAS Discov* **2020,** *25* (9), 963-976.
21. Granborg, J. R.; Handler, A. M.; Janfelt, C., Mass spectrometry imaging in drug distribution and drug metabolism studies – Principles, applications and perspectives. *Trends in Analytical Chemistry* **2022,** *146*.
22. Vaysse, P. M.; Heeren, R. M. A.; Porta, T.; Balluff, B., Mass spectrometry imaging for clinical research - latest developments, applications, and current limitations. *Analyst* **2017,** *142* (15), 2690-2712.

23. Kempson, I. M.; Prestidge, C. A., Mass Spectrometry Imaging of Pharmaceuticals: From Tablets to Tissues. In *Analytical Techniques in the Pharmaceutical Sciences*, Müllertz, A.; Perrie, Y.; Rades, T., Eds. Springer New York: New York, NY, 2016; pp 629-647.
24. Lietz, C. B.; Gemperline, E.; Li, L., Qualitative and quantitative mass spectrometry imaging of drugs and metabolites. *Adv Drug Deliv Rev* **2013,** *65* (8), 1074-85.
25. Gao, S. Q.; Zhao, J. H.; Guan, Y.; Tang, Y. S.; Li, Y.; Liu, L. Y., Mass spectrometry imaging technology in metabolomics: A systematic review. *Biomed Chromatogr* **2022**, e5494.
26. Chughtai, K.; Heeren, R. M., Mass spectrometric imaging for biomedical tissue analysis. *Chem Rev* **2010,** *110* (5), 3237-77.
27. Weaver, E. M.; Hummon, A. B., Imaging mass spectrometry: from tissue sections to cell cultures. *Adv Drug Deliv Rev* **2013,** *65* (8), 1039-55.
28. Spengler, B., Mass spectrometry imaging of biomolecular information. *Analytical chemistry* **2015,** *87* (1), 64-82.
29. Buchberger, A. R.; DeLaney, K.; Johnson, J.; Li, L., Mass Spectrometry Imaging: A Review of Emerging Advancements and Future Insights. *Analytical chemistry* **2018,** *90* (1), 240-265.
30. Dilmetz, B. A.; Lee, Y. R.; Condina, M. R.; Briggs, M.; Young, C.; Desire, C. T.; Klingler-Hoffmann, M.; Hoffmann, P., Novel technical developments in mass spectrometry imaging in 2020: A mini review. *Analytical Science Advances* **2021,** *2* (3-4), 225-237.
31. Heeren, R. M. A., Getting the picture: The coming of age of imaging MS. *International Journal of Mass Spectrometry* **2015,** *377*, 672-680.
32. De Hoffmann, E.; Stroobant, V., *Mass spectrometry: principles and applications*. John Wiley & Sons: 2007.
33. Wang, T.; Cheng, X.; Xu, H.; Meng, Y.; Yin, Z.; Li, X.; Hang, W., Perspective on Advances in Laser-Based High-Resolution Mass Spectrometry Imaging. *Analytical chemistry* **2020,** *92* (1), 543-553.
34. Caprioli, R. M.; Farmer, T. B.; Gile, J., Molecular imaging of biological samples: localization of peptides and proteins using MALDI-TOF MS. *Analytical chemistry* **1997,** *69* (23), 4751-60.
35. Taylor, A. J.; Dexter, A.; Bunch, J., Exploring Ion Suppression in Mass Spectrometry Imaging of a Heterogeneous Tissue. *Analytical chemistry* **2018,** *90* (9), 5637-5645.
36. Goodwin, R. J. A., Sample preparation for mass spectrometry imaging: small mistakes can lead to big consequences. *J Proteomics* **2012,** *75* (16), 4893-4911.
37. Barre, F. P. Y.; Paine, M. R. L.; Flinders, B.; Trevitt, A. J.; Kelly, P. D.; Ait-Belkacem, R.; Garcia, J. P.; Creemers, L. B.; Stauber, J.; Vreeken, R. J.; Cillero-Pastor, B.; Ellis, S. R.; Heeren, R. M. A., Enhanced Sensitivity Using MALDI Imaging Coupled with Laser Postionization (MALDI-2) for Pharmaceutical Research. *Analytical chemistry* **2019,** *91* (16), 10840-10848.
38. Kompauer, M.; Heiles, S.; Spengler, B., Atmospheric pressure MALDI mass spectrometry imaging of tissues and cells at 1.4-μm lateral resolution. *Nature Methods* **2016,** *14* (1), 90-96.
39. Takats, Z.; Wiseman, J. M.; Gologan, B.; Cooks, R. G., Mass spectrometry sampling under ambient conditions with desorption electrospray ionization. *Science* **2004,** *306* (5695), 471-3.
40. Wiseman, J. M.; Ifa, D. R.; Song, Q.; Cooks, R. G., Tissue imaging at atmospheric pressure using desorption electrospray ionization (DESI) mass spectrometry. *Angew Chem Int Ed Engl* **2006,** *45* (43), 7188-92.
41. Tillner, J.; Wu, V.; Jones, E. A.; Pringle, S. D.; Karancsi, T.; Dannhorn, A.; Veselkov, K.; McKenzie, J. S.; Takats, Z., Faster, More Reproducible DESI-MS for Biological Tissue Imaging. *J Am Soc Mass Spectrom* **2017,** *28* (10), 2090-2098.
42. Shi, L.; Habib, A.; Bi, L.; Hong, H.; Begum, R.; Wen, L., Ambient Ionization Mass Spectrometry: Application and Prospective. *Crit Rev Anal Chem* **2022**, 1-50.
43. Dong, Y.; Li, B.; Aharoni, A., More than Pictures: When MS Imaging Meets Histology. *Trends Plant Sci* **2016,** *21* (8), 686-698.
44. Li, L. H.; Hsieh, H. Y.; Hsu, C. C., Clinical Application of Ambient Ionization Mass Spectrometry. *Mass Spectrom (Tokyo)* **2017,** *6* (Spec Iss), S0060.
45. Chandra, S.; Morrison, G. H., Imaging elemental distribution and ion transport in cultured cells with ion microscopy. *Science* **1985,** *228* (4707), 1543-4.

46. Moore, K. L.; Lombi, E.; Zhao, F. J.; Grovenor, C. R., Elemental imaging at the nanoscale: NanoSIMS and complementary techniques for element localisation in plants. *Anal Bioanal Chem* **2012,** *402* (10), 3263-73.
47. Kilburn, M. R.; Clode, P. L., Elemental and Isotopic Imaging of Biological Samples Using NanoSIMS. In *Electron Microscopy*, 2014; pp 733-755.
48. Kilburn, M. R.; Wacey, D., CHAPTER 1. Nanoscale Secondary Ion Mass Spectrometry (NanoSIMS) as an Analytical Tool in the Geosciences. In *Principles and Practice of Analytical Techniques in Geosciences*, 2014; pp 1-34.
49. Hoppe, P.; Cohen, S.; Meibom, A., NanoSIMS: Technical Aspects and Applications in Cosmochemistry and Biological Geochemistry. *Geostandards and Geoanalytical Research* **2013,** *37* (2), 111-154.
50. Gyngard, F.; Steinhauser, M. L., Biological explorations with nanoscale secondary ion mass spectrometry. *Journal of Analytical Atomic Spectrometry* **2019,** *34* (8), 1534-1545.
51. Nuñez, J.; Renslow, R.; Cliff, J. B.; Anderton, C. R., NanoSIMS for biological applications: Current practices and analyses. *Biointerphases* **2018,** *13* (3).
52. Agüi-Gonzalez, P.; Jähne, S.; Phan, N. T. N., SIMS imaging in neurobiology and cell biology. *Journal of Analytical Atomic Spectrometry* **2019,** *34* (7), 1355-1368.
53. Boxer, S. G.; Kraft, M. L.; Weber, P. K., Advances in imaging secondary ion mass spectrometry for biological samples. *Annu Rev Biophys* **2009,** *38*, 53-74.
54. Legin, A. A.; Schintlmeister, A.; Jakupec, M. A.; Galanski, M.; Lichtscheidl, I.; Wagner, M.; Keppler, B. K., NanoSIMS combined with fluorescence microscopy as a tool for subcellular imaging of isotopically labeled platinum-based anticancer drugs. *Chemical Science* **2014,** *5* (8).
55. Jiang, H.; Passarelli, M. K.; Munro, P. M.; Kilburn, M. R.; West, A.; Dollery, C. T.; Gilmore, I. S.; Rakowska, P. D., High-resolution sub-cellular imaging by correlative NanoSIMS and electron microscopy of amiodarone internalisation by lung macrophages as evidence for drug-induced phospholipidosis. *Chemical communications (Cambridge, England)* **2017,** *53* (9), 1506-1509.
56. He, C.; Migawa, M. T.; Chen, K.; Weston, T. A.; Tanowitz, M.; Song, W.; Guagliardo, P.; Iyer, K. S.; Bennett, C. F.; Fong, L. G.; Seth, P. P.; Young, S. G.; Jiang, H., High-resolution visualization and quantification of nucleic acid-based therapeutics in cells and tissues using Nanoscale secondary ion mass spectrometry (NanoSIMS). *Nucleic Acids Res* **2021,** *49* (1), 1-14.
57. Eswara, S.; Pshenova, A.; Yedra, L.; Hoang, Q. H.; Lovric, J.; Philipp, P.; Wirtz, T., Correlative microscopy combining transmission electron microscopy and secondary ion mass spectrometry: A general review on the state-of-the-art, recent developments, and prospects. *Applied Physics Reviews* **2019,** *6* (2), 021312.
58. Thomen, A.; Najafinobar, N.; Penen, F.; Kay, E.; Upadhyay, P. P.; Li, X.; Phan, N. T. N.; Malmberg, P.; Klarqvist, M.; Andersson, S.; Kurczy, M. E.; Ewing, A. G., Subcellular Mass Spectrometry Imaging and Absolute Quantitative Analysis across Organelles. *ACS nano* **2020,** *14* (4), 4316-4325.
59. Zamecnik, P. C.; Stephenson, M. L., Inhibition of Rous sarcoma virus replication and cell transformation by a specific oligodeoxynucleotide. *Proceedings of the National Academy of Sciences of the United States of America* **1978,** *75* (1), 280-4.
60. Stein, C. A.; Castanotto, D., FDA-Approved Oligonucleotide Therapies in 2017. *Mol Ther* **2017,** *25* (5), 1069-1075.
61. Yin, W.; Rogge, M., Targeting RNA: A Transformative Therapeutic Strategy. *Clin Transl Sci* **2019,** *12* (2), 98-112.
62. Crooke, S. T.; Liang, X.-h.; Crooke, R. M.; Baker, B. F.; Geary, R. S., Antisense drug discovery and development technology considered in a pharmacological context. *Biochemical Pharmacology* **2021,** *189*, 114196.
63. Qin, S.; Tang, X.; Chen, Y.; Chen, K.; Fan, N.; Xiao, W.; Zheng, Q.; Li, G.; Teng, Y.; Wu, M.; Song, X., mRNA-based therapeutics: powerful and versatile tools to combat diseases. *Signal Transduct Target Ther* **2022,** *7* (1), 166.
64. Zhu, Y.; Zhu, L.; Wang, X.; Jin, H., RNA-based therapeutics: an overview and prospectus. *Cell Death Dis* **2022,** *13* (7), 644.

65. Crooke, S. T.; Liang, X. H.; Baker, B. F.; Crooke, R. M., Antisense technology: A review. *J Biol Chem* **2021,** *296*, 100416.
66. Roberts, T. C.; Langer, R.; Wood, M. J. A., Advances in oligonucleotide drug delivery. *Nature Reviews Drug Discovery* **2020,** *19* (10), 673-694.
67. Hammond, S. M.; Aartsma-Rus, A.; Alves, S.; Borgos, S. E.; Buijsen, R. A. M.; Collin, R. W. J.; Covello, G.; Denti, M. A.; Desviat, L. R.; Echevarria, L.; Foged, C.; Gaina, G.; Garanto, A.; Goyenvalle, A. T.; Guzowska, M.; Holodnuka, I.; Jones, D. R.; Krause, S.; Lehto, T.; Montolio, M.; Van Roon-Mom, W.; Arechavala-Gomeza, V., Delivery of oligonucleotide-based therapeutics: challenges and opportunities. *EMBO Mol Med* **2021,** *13* (4), e13243.
68. Hu, B.; Zhong, L.; Weng, Y.; Peng, L.; Huang, Y.; Zhao, Y.; Liang, X. J., Therapeutic siRNA: state of the art. *Signal Transduct Target Ther* **2020,** *5* (1), 101.
69. Zhou, J.; Rossi, J., Aptamers as targeted therapeutics: current potential and challenges. *Nature reviews. Drug discovery* **2017,** *16* (3), 181-202.
70. Childs-Disney, J. L.; Yang, X.; Gibaut, Q. M. R.; Tong, Y.; Batey, R. T.; Disney, M. D., Targeting RNA structures with small molecules. *Nature Reviews Drug Discovery* **2022,** *21* (10), 736-762.
71. Martin, C.; De Piccoli, S.; Gaysinski, M.; Becquart, C.; Azoulay, S.; Di Giorgio, A.; Duca, M., Unveiling RNA-Binding Properties of Verapamil and Preparation of New Derivatives as Inhibitors of HIV-1 Tat-TAR Interaction. *ChemPlusChem* **2020,** *85* (1), 207-216.
72. Vo, D. D.; Becquart, C.; Tran, T. P. A.; Di Giorgio, A.; Darfeuille, F.; Staedel, C.; Duca, M., Building of neomycin-nucleobase-amino acid conjugates for the inhibition of oncogenic miRNAs biogenesis. *Org Biomol Chem* **2018,** *16* (34), 6262-6274.
73. Becquart, C.; Le Roch, M.; Azoulay, S.; Uriac, P.; Di Giorgio, A.; Duca, M., Exploring Heterocycle-Spermine Conjugates as Modulators of Oncogenic microRNAs Biogenesis. *ACS Omega* **2018,** *3* (12), 16500-16508.
74. Lieberman, J., Tapping the RNA world for therapeutics. *Nature Structural & Molecular Biology* **2018,** *25* (5), 357-364.
75. Fauman, E. B.; Rai, B. K.; Huang, E. S., Structure-based druggability assessment—identifying suitable targets for small molecule therapeutics. *Current Opinion in Chemical Biology* **2011,** *15* (4), 463-468.
76. Geary, R. S.; Norris, D.; Yu, R.; Bennett, C. F., Pharmacokinetics, biodistribution and cell uptake of antisense oligonucleotides. *Advanced Drug Delivery Reviews* **2015,** *87*, 46-51.
77. Dowdy, S. F., Overcoming cellular barriers for RNA therapeutics. *Nature Biotechnology* **2017,** *35* (3), 222-229.
78. Khvorova, A.; Watts, J. K., The chemical evolution of oligonucleotide therapies of clinical utility. *Nature Biotechnology* **2017,** *35* (3), 238-248.
79. Gokirmak, T.; Nikan, M.; Wiechmann, S.; Prakash, T. P.; Tanowitz, M.; Seth, P. P., Overcoming the challenges of tissue delivery for oligonucleotide therapeutics. *Trends Pharmacol Sci* **2021,** *42* (7), 588-604.
80. Juliano, R. L., The delivery of therapeutic oligonucleotides. *Nucleic Acids Res.* **2016,** *44* (14), 6518-6548.
81. Juliano, R. L., Intracellular Trafficking and Endosomal Release of Oligonucleotides: What We Know and What We Don't. *Nucleic Acid Therapeutics* **2018,** *28* (3), 166-177.
82. Juliano, R. L., Chemical Manipulation of the Endosome Trafficking Machinery: Implications for Oligonucleotide Delivery. *Biomedicines* **2021,** *9* (5).
83. Dowdy, S. F.; Setten, R. L.; Cui, X. S.; Jadhav, S. G., Delivery of RNA Therapeutics: The Great Endosomal Escape! *Nucleic Acid Ther* **2022**.
84. Wan, W. B.; Seth, P. P., The Medicinal Chemistry of Therapeutic Oligonucleotides. *J Med Chem* **2016,** *59* (21), 9645-9667.
85. Crooke, S. T.; Witztum, J. L.; Bennett, C. F.; Baker, B. F., RNA-Targeted Therapeutics. *Cell Metab* **2018,** *27* (4), 714-739.

86. Quemener, A. M.; Bachelot, L.; Forestier, A.; Donnou-Fournet, E.; Gilot, D.; Galibert, M. D., The powerful world of antisense oligonucleotides: From bench to bedside. *Wiley Interdiscip Rev RNA* **2020,** *11* (5), e1594.
87. Quemener, A. M.; Centomo, M. L.; Sax, S. L.; Panella, R., Small Drugs, Huge Impact: The Extraordinary Impact of Antisense Oligonucleotides in Research and Drug Development. *Molecules* **2022,** *27* (2).
88. Crooke, S. T., Molecular Mechanisms of Antisense Oligonucleotides. *Nucleic Acid Ther* **2017,** *27* (2), 70-77.
89. Vickers, T. A.; Crooke, S. T., The rates of the major steps in the molecular mechanism of RNase H1-dependent antisense oligonucleotide induced degradation of RNA. *Nucleic Acids Res* **2015,** *43* (18), 8955-63.
90. Dhuri, K.; Bechtold, C.; Quijano, E.; Pham, H.; Gupta, A.; Vikram, A.; Bahal, R., Antisense Oligonucleotides: An Emerging Area in Drug Discovery and Development. *J Clin Med* **2020,** *9* (6).
91. Bennett, C. F.; Swayze, E. E., RNA Targeting Therapeutics: Molecular Mechanisms of Antisense Oligonucleotides as a Therapeutic Platform. *Annual Review of Pharmacology and Toxicology* **2010,** *50* (1), 259-293.
92. Walder, R. Y.; Walder, J. A., Role of RNase H in hybrid-arrested translation by antisense oligonucleotides. *Proceedings of the National Academy of Sciences of the United States of America* **1988,** *85* (14), 5011-5.
93. Havens, M. A.; Hastings, M. L., Splice-switching antisense oligonucleotides as therapeutic drugs. *Nucleic Acids Res* **2016,** *44* (14), 6549-63.
94. Debacker, A. J.; Voutila, J.; Catley, M.; Blakey, D.; Habib, N., Delivery of Oligonucleotides to the Liver with GalNAc: From Research to Registered Therapeutic Drug. *Molecular Therapy* **2020**.
95. Eckstein, F., Phosphorothioates, Essential Components of Therapeutic Oligonucleotides. *Nucleic Acid Therapeutics* **2014,** *24* (6), 374-387.
96. Crooke, S. T.; Vickers, T. A.; Liang, X. H., Phosphorothioate modified oligonucleotide-protein interactions. *Nucleic Acids Res.* **2020**.
97. Crooke, S.; Seth, P. P.; Vickers, T. A.; Liang, X.-h., The Interaction of Phosphorothioate Containing RNA Targeted Drugs with Proteins is a Critical Determinant of The Therapeutic Effects of These Agents. *Journal of the American Chemical Society* **2020**.
98. Bennett, C. F.; Baker, B. F.; Pham, N.; Swayze, E.; Geary, R. S., Pharmacology of Antisense Drugs. *Annu Rev Pharmacol Toxicol* **2017,** *57*, 81-105.
99. Ostergaard, M. E.; De Hoyos, C. L.; Wan, W. B.; Shen, W.; Low, A.; Berdeja, A.; Vasquez, G.; Murray, S.; Migawa, M. T.; Liang, X. H.; Swayze, E. E.; Crooke, S. T.; Seth, P. P., Understanding the effect of controlling phosphorothioate chirality in the DNA gap on the potency and safety of gapmer antisense oligonucleotides. *Nucleic Acids Res* **2020,** *48* (4), 1691-1700.
100. Moore, L. D.; Le, T.; Fan, G., DNA methylation and its basic function. *Neuropsychopharmacology* **2013,** *38* (1), 23-38.
101. Chappell, A. E.; Gaus, H. J.; Berdeja, A.; Gupta, R.; Jo, M.; Prakash, T. P.; Oestergaard, M.; Swayze, E. E.; Seth, P. P., Mechanisms of palmitic acid-conjugated antisense oligonucleotide distribution in mice. *Nucleic Acids Res* **2020,** *48* (8), 4382-4395.
102. Prakash, T. P.; Mullick, A. E.; Lee, R. G.; Yu, J.; Yeh, S. T.; Low, A.; Chappell, A. E.; Ostergaard, M. E.; Murray, S.; Gaus, H. J.; Swayze, E. E.; Seth, P. P., Fatty acid conjugation enhances potency of antisense oligonucleotides in muscle. *Nucleic Acids Res* **2019,** *47* (12), 6029-6044.
103. Benizri, S.; Gissot, A.; Martin, A.; Vialet, B.; Grinstaff, M. W.; Barthelemy, P., Bioconjugated Oligonucleotides: Recent Developments and Therapeutic Applications. *Bioconjug Chem* **2019,** *30* (2), 366-383.
104. Bon, C.; Hofer, T.; Bousquet-Mélou, A.; Davies, M. R.; Krippendorff, B.-F., Capacity limits of asialoglycoprotein receptor-mediated liver targeting. *mAbs* **2017,** *9* (8), 1360-1369.
105. D'Souza, A. A.; Devarajan, P. V., Asialoglycoprotein receptor mediated hepatocyte targeting - strategies and applications. *J Control Release* **2015,** *203*, 126-39.
106. Grewal, P. K., The Ashwell–Morell Receptor. In *Functional Glycomics*, 2010; pp 223-241.

107. Prakash, T. P.; Graham, M. J.; Yu, J.; Carty, R.; Low, A.; Chappell, A.; Schmidt, K.; Zhao, C.; Aghajan, M.; Murray, H. F.; Riney, S.; Booten, S. L.; Murray, S. F.; Gaus, H.; Crosby, J.; Lima, W. F.; Guo, S.; Monia, B. P.; Swayze, E. E.; Seth, P. P., Targeted delivery of antisense oligonucleotides to hepatocytes using triantennaryN-acetyl galactosamine improves potency 10-fold in mice. *Nucleic Acids Res.* **2014,** *42* (13), 8796-8807.
108. Knerr, L.; Prakash, T. P.; Lee, R.; Drury Iii, W. J.; Nikan, M.; Fu, W.; Pirie, E.; Maria, L.; Valeur, E.; Hayen, A.; Olwegard-Halvarsson, M.; Broddefalk, J.; Ammala, C.; Ostergaard, M. E.; Meuller, J.; Sundstrom, L.; Andersson, P.; Janzen, D.; Jansson-Lofmark, R.; Seth, P. P.; Andersson, S., Glucagon Like Peptide 1 Receptor Agonists for Targeted Delivery of Antisense Oligonucleotides to Pancreatic Beta Cell. *J. Am. Chem. Soc.* **2021,** *143* (9), 3416-3429.
109. Ammala, C.; Drury, W. J., 3rd; Knerr, L.; Ahlstedt, I.; Stillemark-Billton, P.; Wennberg-Huldt, C.; Andersson, E. M.; Valeur, E.; Jansson-Lofmark, R.; Janzen, D.; Sundstrom, L.; Meuller, J.; Claesson, J.; Andersson, P.; Johansson, C.; Lee, R. G.; Prakash, T. P.; Seth, P. P.; Monia, B. P.; Andersson, S., Targeted delivery of antisense oligonucleotides to pancreatic beta-cells. *Sci Adv* **2018,** *4* (10), eaat3386.
110. Crooke, S. T.; Wang, S.; Vickers, T. A.; Shen, W.; Liang, X. H., Cellular uptake and trafficking of antisense oligonucleotides. *Nature Biotechnology* **2017,** *35* (3), 230-237.
111. Dowdy, S. F., Endosomal escape of RNA therapeutics: How do we solve this rate-limiting problem? *Rna* **2023**.
112. Tanowitz, M.; Hettrick, L.; Revenko, A.; Kinberger, G. A.; Prakash, T. P.; Seth, P. P., Asialoglycoprotein receptor 1 mediates productive uptake of N-acetylgalactosamine-conjugated and unconjugated phosphorothioate antisense oligonucleotides into liver hepatocytes. *Nucleic Acids Res* **2017,** *45* (21), 12388-12400.
113. Du Rietz, H.; Hedlund, H.; Wilhelmson, S.; Nordenfelt, P.; Wittrup, A., Imaging small molecule-induced endosomal escape of siRNA. *Nature communications* **2020,** *11* (1), 1809.
114. Bost, J. P.; Ojansivu, M.; Munson, M. J.; Wesen, E.; Gallud, A.; Gupta, D.; Gustafsson, O.; Saher, O.; Radler, J.; Higgins, S. G.; Lehto, T.; Holme, M. N.; Dahlen, A.; Engkvist, O.; Stromstedt, P. E.; Andersson, S.; Edvard Smith, C. I.; Stevens, M. M.; Esbjorner, E. K.; Collen, A.; El Andaloussi, S., Novel endosomolytic compounds enable highly potent delivery of antisense oligonucleotides. *Commun Biol* **2022,** *5* (1), 185.
115. Deprey, K.; Batistatou, N.; Kritzer, J. A., A critical analysis of methods used to investigate the cellular uptake and subcellular localization of RNA therapeutics. *Nucleic Acids Res* **2020**.
116. Castanotto, D.; Lin, M.; Kowolik, C.; Wang, L.; Ren, X. Q.; Soifer, H. S.; Koch, T.; Hansen, B. R.; Oerum, H.; Armstrong, B.; Wang, Z.; Bauer, P.; Rossi, J.; Stein, C. A., A cytoplasmic pathway for gapmer antisense oligonucleotide-mediated gene silencing in mammalian cells. *Nucleic Acids Res* **2015,** *43* (19), 9350-61.
117. Gonzalez-Barriga, A.; Nillessen, B.; Kranzen, J.; van Kessel, I. D. G.; Croes, H. J. E.; Aguilera, B.; de Visser, P. C.; Datson, N. A.; Mulders, S. A. M.; van Deutekom, J. C. T.; Wieringa, B.; Wansink, D. G., Intracellular Distribution and Nuclear Activity of Antisense Oligonucleotides After Unassisted Uptake in Myoblasts and Differentiated Myotubes In Vitro. *Nucleic Acid Ther* **2017,** *27* (3), 144-158.
118. Mukherjee, P.; Aksamitiene, E.; Alex, A.; Shi, J.; Bera, K.; Zhang, C.; Spillman, D. R.; Marjanovic, M.; Fazio, M.; Seth, P. P.; Frazier, K.; Hood, S. R.; Boppart, S. A., Differential Uptake of Antisense Oligonucleotides in Mouse Hepatocytes and Macrophages Revealed by Simultaneous Two-Photon Excited Fluorescence and Coherent Raman Imaging. *Nucleic Acid Ther* **2022,** *32* (3), 163-176.
119. Finicle, B. T.; Eckenstein, K. H.; Revenko, A. S.; Anderson, B. A.; Wan, W. B.; McCracken, A. N.; Gil, D.; Fruman, D. A.; Hanessian, S.; Seth, P. P.; Edinger, A. L., Simultaneous inhibition of endocytic recycling and lysosomal fusion sensitizes cells and tissues to oligonucleotide therapeutics. *Nucleic Acids Res* **2023**.
120. Buntz, A.; Killian, T.; Schmid, D.; Seul, H.; Brinkmann, U.; Ravn, J.; Lindholm, M.; Knoetgen, H.; Haucke, V.; Mundigl, O., Quantitative fluorescence imaging determines the absolute number of locked nucleic acid oligonucleotides needed for suppression of target gene expression. *Nucleic Acids Res* **2019,** *47* (2), 953-969.

121. Wang, S.; Allen, N.; Prakash, T. P.; Liang, X. H.; Crooke, S. T., Lipid Conjugates Enhance Endosomal Release of Antisense Oligonucleotides Into Cells. *Nucleic Acid Ther* **2019,** *29* (5), 245-255.
122. Wang, S.; Sun, H.; Tanowitz, M.; Liang, X. H.; Crooke, S. T., Intra-endosomal trafficking mediated by lysobisphosphatidic acid contributes to intracellular release of phosphorothioate-modified antisense oligonucleotides. *Nucleic Acids Res* **2017,** *45* (9), 5309-5322.
123. Liang, X.-h.; Nichols, J. G.; Tejera, D.; Crooke, S. T., Perinuclear positioning of endosomes can affect PS-ASO activities. *Nucleic Acids Res.* **2021,** *49* (22), 12970-12985.
124. Lacroix, A.; Vengut-Climent, E.; de Rochambeau, D.; Sleiman, H. F., Uptake and Fate of Fluorescently Labeled DNA Nanostructures in Cellular Environments: A Cautionary Tale. *ACS Cent Sci* **2019,** *5* (5), 882-891.
125. Linnane, E.; Davey, P.; Zhang, P.; Puri, S.; Edbrooke, M.; Chiarparin, E.; Revenko, A. S.; Macleod, A. R.; Norman, J. C.; Ross, S. J., Differential uptake, kinetics and mechanisms of intracellular trafficking of next-generation antisense oligonucleotides across human cancer cell lines. *Nucleic Acids Res* **2019,** *47* (9), 4375-4392.
126. Scharner, J.; Qi, S.; Rigo, F.; Bennett, C. F.; Krainer, A. R., Delivery of GalNAc-Conjugated Splice-Switching ASOs to Non-hepatic Cells through Ectopic Expression of Asialoglycoprotein Receptor. *Mol Ther Nucleic Acids* **2019,** *16*, 313-325.
127. Weidolf, L.; Bjorkbom, A.; Dahlen, A.; Elebring, M.; Gennemark, P.; Holtta, M.; Janzen, D.; Li, X.; Andersson, S., Distribution and biotransformation of therapeutic antisense oligonucleotides and conjugates. *Drug discovery today* **2021,** *26* (10), 2244-2258.
128. Kaczmarkiewicz, A.; Nuckowski, L.; Studzinska, S.; Buszewski, B., Analysis of Antisense Oligonucleotides and Their Metabolites with the Use of Ion Pair Reversed-Phase Liquid Chromatography Coupled with Mass Spectrometry. *Crit Rev Anal Chem* **2019,** *49* (3), 256-270.
129. Pendergraff, H.; Schmidt, S.; Vikesa, J.; Weile, C.; Overup, C.; M, W. L.; Koch, T., Nuclear and Cytoplasmatic Quantification of Unconjugated, Label-Free Locked Nucleic Acid Oligonucleotides. *Nucleic Acid Ther* **2020,** *30* (1), 4-13.
130. Nguyen, T. D. K.; Mellander, L.; Lork, A.; Thomen, A.; Philipsen, M.; Kurczy, M. E.; Phan, N. T. N.; Ewing, A. G., Visualization of Partial Exocytotic Content Release and Chemical Transport into Nanovesicles in Cells. *ACS nano* **2022,** *16* (3), 4831-4842.
131. Rabasco, S.; Nguyen, T. D. K.; Gu, C.; Kurczy, M. E.; Phan, N. T. N.; Ewing, A. G., Localization and Absolute Quantification of Dopamine in Discrete Intravesicular Compartments Using NanoSIMS Imaging. *Int J Mol Sci* **2021,** *23* (1).
132. Rabasco, S.; Lork, A. A.; Berlin, E.; Nguyen, T. D. K.; Ernst, C.; Locker, N.; Ewing, A. G.; Phan, N. T. N., Characterization of Stress Granule Protein Turnover in Neuronal Progenitor Cells Using Correlative STED and NanoSIMS Imaging. *Int J Mol Sci* **2023,** *24* (3).
133. Newbury, D. E., Methods for quantitative analysis in secondary ion mass spectrometry. *Scanning* **1980,** *3* (2), 110-118.
134. Jeusset, J.; Stelly, N.; Briancon, C.; Halpern, S.; Roshani, M.; Fragu, P., Signal standardization of the secondary ion mass spectrometry (SIMS) microscope for quantification of halogens and calcium in biological applications. *J Microsc* **1995,** *179* (Pt 3), 314-20.
135. Davission, M. W., P.; Pett-Ridge, J.; Singer, S., Development of Standards for NanoSIMS Analyses of Biological Materials Materials. *LLNL-TR-406039; Lawrence Livermore National Lab (LLNL):Livermore, CA, USA.* **2008**.
136. Levi-Setti, R.; Chabala, J. M.; Gavrilov, K.; Espinosa, R., 3rd; Le Beau, M. M., Imaging of BrdU-labeled human metaphase chromosomes with a high resolution scanning ion microprobe. *Microsc Res Tech* **1997,** *36* (4), 301-12.
137. Berry, J. P.; Galle, P.; Chassoux, D.; Escaig, F.; Linarez-Cruz, L. G.; Lespinats, G., Mapping of intracellular halogenous molecules by low and high resolution SIMS microscopy. *Biol Cell* **1992,** *74* (1), 93-8.
138. Cui, H.; Zhu, X.; Li, S.; Wang, P.; Fang, J., Liver-Targeted Delivery of Oligonucleotides with N-Acetylgalactosamine Conjugation. *ACS Omega* **2021,** *6* (25), 16259-16265.

139. Stulz, R.; Milligan, F.; Stovold, C.; Love, I.; Strömberg, R.; Andersson, S.; Dahlén, A., (34)S-SIL of PCSK9-Active Oligonucleotide as Tools for Accurate Quantification by Mass Spectrometry. *Nucleic Acid Ther* **2021,** *31* (5), 375-381.
140. Stulz, R.; Meuller, J.; Bazdarevic, D.; Wennberg Huldt, C.; Stromberg, R.; Andersson, S.; Dahlen, A., A Versatile and Convenient Synthesis of (34) S-Labeled Phosphorothioate Oligonucleotides. *Chembiochem* **2018,** *19* (19), 2114-2119.
141. Kay, E.; Stulz, R.; Becquart, C.; Lovric, J.; Tangemo, C.; Thomen, A.; Bazdarevic, D.; Najafinobar, N.; Dahlen, A.; Pielach, A.; Fernandez-Rodriguez, J.; Stromberg, R.; Ammala, C.; Andersson, S.; Kurczy, M., NanoSIMS Imaging Reveals the Impact of Ligand-ASO Conjugate Stability on ASO Subcellular Distribution. *Pharmaceutics* **2022,** *14* (2), 463.
142. Becquart, C.; Stulz, R.; Thomen, A.; Dost, M.; Najafinobar, N.; Dahlen, A.; Andersson, S.; Ewing, A. G.; Kurczy, M. E., Intracellular Absolute Quantification of Oligonucleotide Therapeutics by NanoSIMS. *Analytical chemistry* **2022,** *94* (29), 10549-10556.
143. Aoki, Y.; Rocha, C. S. J.; Lehto, T.; Miyatake, S.; Johansson, H.; Hashimoto, Y.; Nordin, J. Z.; Mager, I.; Aoki, M.; Graham, M.; Sathyaprakash, C.; Roberts, T. C.; Wood, M. J. A.; Behlke, M. A.; Andaloussi, S. E., Fine Tuning of Phosphorothioate Inclusion in 2'-O-Methyl Oligonucleotides Contributes to Specific Cell Targeting for Splice-Switching Modulation. *Front Physiol* **2021,** *12*, 689179.
144. Sun, Y.; Ma, L., New Insights into Long Non-Coding RNA MALAT1 in Cancer and Metastasis. *Cancers (Basel)* **2019,** *11* (2).
145. Arun, G.; Aggarwal, D.; Spector, D. L., MALAT1 Long Non-Coding RNA: Functional Implications. *Noncoding RNA* **2020,** *6* (2).
146. Mahpour, A.; Mullen, A. C., Our emerging understanding of the roles of long non-coding RNAs in normal liver function, disease, and malignancy. *JHEP Rep* **2021,** *3* (1), 100177.
147. Ganguly, N.; Chakrabarti, S., Role of long noncoding RNAs and related epigenetic mechanisms in liver fibrosis (Review). *Int J Mol Med* **2021,** *47* (3).
148. Amodio, N.; Raimondi, L.; Juli, G.; Stamato, M. A.; Caracciolo, D.; Tagliaferri, P.; Tassone, P., MALAT1: a druggable long non-coding RNA for targeted anti-cancer approaches. *J Hematol Oncol* **2018,** *11* (1), 63-63.
149. Zhang, X.; Hamblin, M. H.; Yin, K. J., The long noncoding RNA Malat1: Its physiological and pathophysiological functions. *RNA Biol* **2017,** *14* (12), 1705-1714.
150. Yan, C.; Chen, J.; Chen, N., Long noncoding RNA MALAT1 promotes hepatic steatosis and insulin resistance by increasing nuclear SREBP-1c protein stability. *Sci Rep* **2016,** *6*, 22640.
151. Maruyama, R.; Yokota, T., Knocking Down Long Noncoding RNAs Using Antisense Oligonucleotide Gapmers. *Methods in molecular biology (Clifton, N.J.)* **2020,** *2176*, 49-56.
152. Iwashita, S.; Shoji, T.; Koizumi, M., Evaluating the Knockdown Activity of MALAT1 ENA Gapmers In Vitro. *Methods in molecular biology (Clifton, N.J.)* **2020,** *2176*, 155-161.
153. Bridges, M. C.; Daulagala, A. C.; Kourtidis, A., LNCcation: lncRNA localization and function. *J Cell Biol* **2021,** *220* (2).
154. Carlevaro-Fita, J.; Rahim, A.; Guigo, R.; Vardy, L. A.; Johnson, R., Cytoplasmic long noncoding RNAs are frequently bound to and degraded at ribosomes in human cells. *RNA* **2016,** *22* (6), 867-82.
155. Wilusz, J. E., Long noncoding RNAs: Re-writing dogmas of RNA processing and stability. *Biochimica et biophysica acta* **2016,** *1859* (1), 128-138.
156. Miller, C. M.; Tanowitz, M.; Donner, A. J.; Prakash, T. P.; Swayze, E. E.; Harris, E. N.; Seth, P. P., Receptor-Mediated Uptake of Phosphorothioate Antisense Oligonucleotides in Different Cell Types of the Liver. *Nucleic Acid Therapeutics* **2018,** *28* (3), 119-127.
157. Schmidt, K.; Prakash, T. P.; Donner, A. J.; Kinberger, G. A.; Gaus, H. J.; Low, A.; Ostergaard, M. E.; Bell, M.; Swayze, E. E.; Seth, P. P., Characterizing the effect of GalNAc and phosphorothioate backbone on binding of antisense oligonucleotides to the asialoglycoprotein receptor. *Nucleic Acids Res* **2017,** *45* (5), 2294-2306.
158. Koller, E.; Vincent, T. M.; Chappell, A.; De, S.; Manoharan, M.; Bennett, C. F., Mechanisms of single-stranded phosphorothioate modified antisense oligonucleotide accumulation in hepatocytes. *Nucleic Acids Res* **2011,** *39* (11), 4795-807.

159. Geary, R. S.; Wancewicz, E.; Matson, J.; Pearce, M.; Siwkowski, A.; Swayze, E.; Bennett, F., Effect of dose and plasma concentration on liver uptake and pharmacologic activity of a 2′-methoxyethyl modified chimeric antisense oligonucleotide targeting PTEN. *Biochemical Pharmacology* **2009,** *78* (3), 284-291.
160. Bonifacino, J. S.; Neefjes, J., Moving and positioning the endolysosomal system. *Curr Opin Cell Biol* **2017,** *47*, 1-8.
161. Miller, C. M.; Donner, A. J.; Blank, E. E.; Egger, A. W.; Kellar, B. M.; Østergaard, M. E.; Seth, P. P.; Harris, E. N., Stabilin-1 and Stabilin-2 are specific receptors for the cellular internalization of phosphorothioate-modified antisense oligonucleotides (ASOs) in the liver. *Nucleic Acids Res.* **2016,** *44* (6), 2782-2794.
162. Lima, W. F.; Vickers, T. A.; Nichols, J.; Li, C.; Crooke, S. T., Defining the factors that contribute to on-target specificity of antisense oligonucleotides. *PLoS One* **2014,** *9* (7), e101752.
163. Wisniewski, J. R.; Vildhede, A.; Noren, A.; Artursson, P., In-depth quantitative analysis and comparison of the human hepatocyte and hepatoma cell line HepG2 proteomes. *J Proteomics* **2016,** *136*, 234-47.
164. Lodish, H.; Berk, A.; Kaiser, C. A.; Kaiser, C.; Krieger, M.; Scott, M. P.; Bretscher, A.; Ploegh, H.; Matsudaira, P., *Molecular cell biology*. Macmillan: 2008.
165. Muller, T. D.; Finan, B.; Bloom, S. R.; D'Alessio, D.; Drucker, D. J.; Flatt, P. R.; Fritsche, A.; Gribble, F.; Grill, H. J.; Habener, J. F.; Holst, J. J.; Langhans, W.; Meier, J. J.; Nauck, M. A.; Perez-Tilve, D.; Pocai, A.; Reimann, F.; Sandoval, D. A.; Schwartz, T. W.; Seeley, R. J.; Stemmer, K.; Tang-Christensen, M.; Woods, S. C.; DiMarchi, R. D.; Tschop, M. H., Glucagon-like peptide 1 (GLP-1). *Mol Metab* **2019,** *30*, 72-130.
166. Huotari, J.; Helenius, A., Endosome maturation. *EMBO J* **2011,** *30* (17), 3481-500.
167. Scott, C. C.; Vacca, F.; Gruenberg, J., Endosome maturation, transport and functions. *Seminars in cell & developmental biology* **2014,** *31*, 2-10.
168. Gruenberg, J., Life in the lumen: The multivesicular endosome. **2020,** *21* (1), 76-93.
169. Leunissen, E. H. P.; Meuleners, M. H. L.; Verkade, J. M. M.; Dommerholt, J.; Hoenderop, J. G. J.; van Delft, F. L., Copper-Free Click Reactions with Polar Bicyclononyne Derivatives for Modulation of Cellular Imaging. *ChemBioChem* **2014,** *15* (10), 1446-1451.
170. Dommerholt, J.; Schmidt, S.; Temming, R.; Hendriks, L. J. A.; Rutjes, F. P. J. T.; van Hest, J. C. M.; Lefeber, D. J.; Friedl, P.; van Delft, F. L., Readily Accessible Bicyclononynes for Bioorthogonal Labeling and Three-Dimensional Imaging of Living Cells. **2010,** *49* (49), 9422-9425.
171. Kuo, C.; Nikan, M.; Yeh, S. T.; Chappell, A. E.; Tanowitz, M.; Seth, P. P.; Prakash, T. P.; Mullick, A. E., Targeted Delivery of Antisense Oligonucleotides Through Angiotensin Type 1 Receptor. *Nucleic Acid Ther* **2022,** *32* (4), 300-311.
172. Seth, P. P.; Tanowitz, M.; Bennett, C. F., Selective tissue targeting of synthetic nucleic acid drugs. *The Journal of Clinical Investigation* **2019,** *129* (3), 915-925.
173. Dowdy, S. F.; Levy, M., RNA Therapeutics (Almost) Comes of Age: Targeting, Delivery and Endosomal Escape. *Nucleic Acid Ther* **2018,** *28* (3), 107-108.
174. Benedetto Tiz, D.; Bagnoli, L.; Rosati, O.; Marini, F.; Sancineto, L.; Santi, C., New Halogen-Containing Drugs Approved by FDA in 2021: An Overview on Their Syntheses and Pharmaceutical Use. *Molecules* **2022,** *27* (5).
175. Setten, R. L.; Rossi, J. J.; Han, S. P., The current state and future directions of RNAi-based therapeutics. *Nature reviews. Drug discovery* **2019,** *18* (6), 421-446.
176. Watts, J. K.; Corey, D. R., Silencing disease genes in the laboratory and the clinic. *J Pathol* **2012,** *226* (2), 365-79.
177. Halloy, F.; Biscans, A.; Bujold, K. E.; Debacker, A.; Hill, A. C.; Lacroix, A.; Luige, O.; Stromberg, R.; Sundstrom, L.; Vogel, J.; Ghidini, A., Innovative developments and emerging technologies in RNA therapeutics. *RNA Biol* **2022,** *19* (1), 313-332.